# BIFURCATING MACH SHOCK REFLECTIONS WITH APPLICATION TO DETONATION STRUCTURE

Philip Mach

A thesis submitted to the Faculty of Graduate and Postdoctoral Studies
in partial fulfillment of the requirements for the degree of

**MASTER OF APPLIED SCIENCE**

in Mechanical Engineering

Ottawa-Carleton Institute for Mechanical and Aerospace Engineering
University of Ottawa
Ottawa, Canada

August 2011

## Abstract

Numerical simulations of Mach shock reflections have shown that the Mach stem can bifurcate as a result of the slip line jetting forward. Numerical simulations were conducted in this study which determined that these bifurcations occur when the Mach number is high, the ramp angle is high, and specific heat ratio is low. It was clarified that the bifurcation is a result of a sufficiently large velocity difference across the slip line which drives the jet. This bifurcation phenomenon has also been observed after triple point collisions in detonation simulations. A triple point reflection was modelled as an inert shock reflecting off a wedge, and the accuracy of the model at early times after reflection indicates that bifurcations in detonations are a result of the shock reflection process. Further investigations revealed that bifurcations likely contribute to the irregular structure observed in certain detonations.

# Acknowledgements

Firstly, I would like to thank my supervisor, Matei Radulescu, who guided me through the complicated task of learning about the detonation phenomenon, provided me with most of the scripts for the numerical simulations, answered my questions (no matter how dumb they were), and was patient with my progress. I would have obviously been lost without him.

I would also like to thank Sheming Lau-Chapdelaine, who studied shock bifurcations for his undergraduate thesis, and Andrea Papi, who studied reactive shock reflections as a summer student. My work was simply a continuation of the work they started.

Finally, I would like to thank the University of Ottawa and the Department of Mechanical Engineering for providing the funding which enabled me to focus on the research. Part of the work was supported by an NSERC discovery grant given to Matei Radulescu.

# Table of Contents

## List of Figures

# List of Tables

# Nomenclature

***SI Units***

***Latin letters***

| | | |
|---|---|---|
| $E_a$ | activation energy | J/kg |
| $k$ | pre-exponential factor in Arrhenius reaction rate law | 1/s |
| $lmax$ | maximum number of grid levels (a parameter used by the AMRITA CFD package) | |
| $M$ | flow Mach number | |
| $M_{CJ}$ | CJ Mach number | |
| $M_s$ | Mach number of incident shock | |
| $M_{sd}$ | Mach number of incident shock at time of triple point reflection in detonations | |
| $p$ | pressure | Pa |
| $Q$ | heat of reaction | J/Kg |
| $r$ | refinement ratio (a parameter used by the AMRITA CFD package) | |
| $R$ | specific gas constant | J/kg·K |
| $t$ | Time | s |
| $T$ | Temperature | K |
| $u$ | velocity in lab frame of reference | m/s |
| $v$ | velocity in shock or triple point frame of reference | m/s |
| $x$ | axis coordinate in direction of shock or detonation propagation | m |
| $y$ | axis coordinate transverse to shock or detonation propagation | m |

***Greek letters***

| | | |
|---|---|---|
| $\gamma$ | specific heat ratio | |
| $\Delta_{1/2}$ | ZND half-reaction length | m |
| $\theta$ | inclination angle of incident shock at time of triple point reflection in detonations | |
| $\theta_i$ | deflection angle of flow after passing across a shock into state (i) | |
| $\theta_w$ | ramp angle | |

| | | |
|---|---|---|
| $\lambda$ | reaction progress variable | |
| $\rho$ | density | Kg/m$^3$ |
| $\varphi_i$ | angle of incidence of flow before passing across a shock into state (i) | |
| $\chi$ | triple point trajectory angle (with respect to the ramp) | |

### *Subscripts*

| | |
|---|---|
| 0 | state ahead of the incident shock wave or detonation wave |
| 1 | state behind the incident shock wave |
| 2 | state behind the reflected shock wave, r |
| 3 | state behind the Mach stem, m |
| n | velocity component normal to the Mach shock |
| VN | the von Neumann state (post shock state in a ZND detonation wave) |

### *Superscripts*

| | |
|---|---|
| ’ | refers to the second triple point in a Double Mach Reflection or the post reflection triple point in Oppenheim’s model for symmetric triple point reflections of detonations presented in Section 3.1 |

### *Abbreviations*

| | |
|---|---|
| B | point where an imaginary straight slip line, ss, would hit the wall in a Mach reflection |
| i | incident shock |
| k | bifurcation triple point |
| K | kink observed in Transitional Mach reflection |
| m | Mach shock |
| r | reflected shock |
| s | slip line |
| ss | imaginary straight slip line |
| T | triple point |

### *Acronyms*

| | |
|---|---|
| CFD | computational fluid dynamics |

| | |
|---|---|
| CJ | Chapman-Jouguet |
| ZND | Zeldovich-von Neumann-Doering |

### ***Specialized terms***

| | |
|---|---|
| Bifurcation | the splitting of the Mach shock into two segments, and thus the formation of a new triple, k |
| Slip line | term used to describe the contact surface between the flow in state 2 and 3 in a Mach reflection |

# 1 Introduction

## 1.1 Shock reflections

When a moving shock interacts with an inclined wedge (see Figure 1), it experiences a process known as unsteady shock reflection, which we will simply refer to as shock reflection. Blast waves (decaying shock waves originating from explosions) and detonation waves (shock waves supported by an exothermic reaction) are two common sources of moving shock waves. Therefore, shock reflections can occur when blast waves or detonation waves interact with a reflective surface.

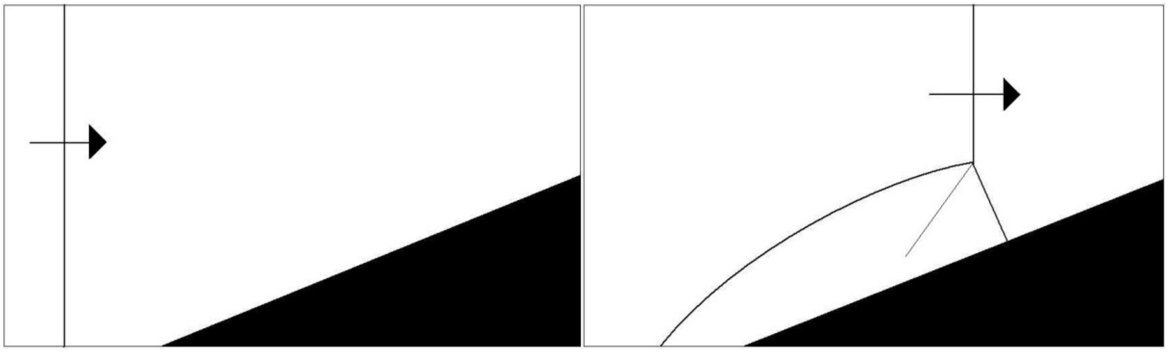

**Figure 1: Sketch of a moving shock before (left) and during (right) an interaction with an inclined wedge.**

Depending on the shock reflection parameters (Mach number of the incident shock, $M_s$; ratio of specific heats, $\gamma$; and wedge angle, $\theta_w$), the shock reflection can take on a number of different configurations. Ben-Dor (2007) provides a good review of these configurations. There are two general shock reflection configurations that are possible: regular and irregular reflections. A regular reflection consists of an incident shock and a reflected shock (see Figure 2a), and is observed when the wedge angle is sufficiently large. An irregular reflection has a Mach stem (also called Mach shock) in addition to the incident and reflected shocks. Within the irregular reflection regime, there are two general shock configurations that are possible: a Von Neumann reflection, or a Mach reflection. The Mach stem in a Von Neumann reflection merges smoothly with the incident shock, and the reflected shock is actually not a shock but a band of compression waves. Von Neumann reflections only occur when weak incident shocks reflect off of small wedge angles. When the shock is sufficiently strong, or the ramp angle is sufficiently large, the reflected shock is indeed a shock, and the three shocks meet at a well-defined triple point. This configuration is known as a Mach reflection (see Figure 2b). For Mach reflections, a contact surface forms between the fluid that is processed by the incident and reflected shock, and the fluid that is processed by the Mach stem. In this thesis, we will call this contact surface the slip line. For more details on the shock reflection configurations, see Ben-Dor (2007).

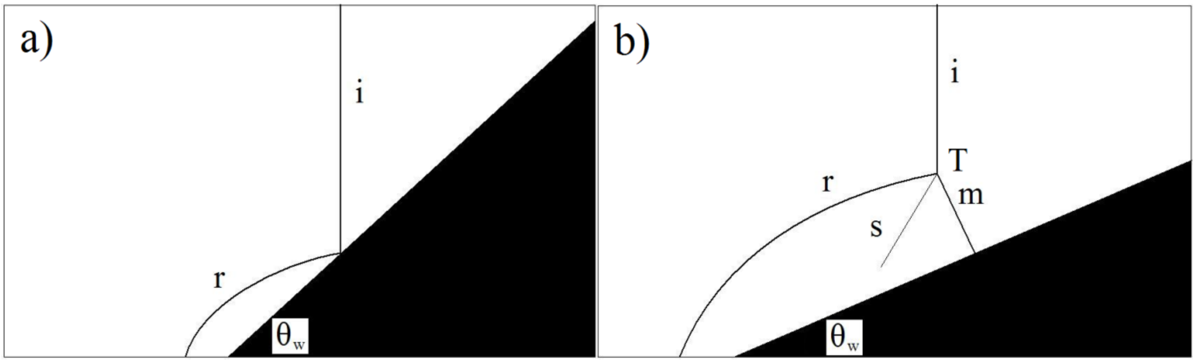

**Figure 2: Sketch of a) a regular reflection and b) a Mach reflection. i indicates the incident shock, r indicates the reflected shock, m indicates the Mach shock, T indicates the triple point, and s indicates the slip line.**

It has been observed that the slip line formed by Mach reflections can jet forward towards the Mach stem. Under certain conditions, this forward jetting slip line can be sufficiently strong as to form a vortex which causes the base of the Mach stem to protrude forward. Numerical simulations conducted by Colella and Glaz (1985) show that the protrusion can be so strong that the Mach stem actually bifurcates, and thus a new triple point forms, as sketched in Figure 3. Experimental evidence of this bifurcation phenomenon exists: one of the shadowgraph images of the shock reflection experiments conducted by Semenov et al. (2009), shown in Figure 4, reveals a bifurcation. In depth studies of this bifurcating shock reflection regime have yet to be conducted. Therefore, the first part of this study will address this regime. Specifically, it will try to clarify when these bifurcations occur.

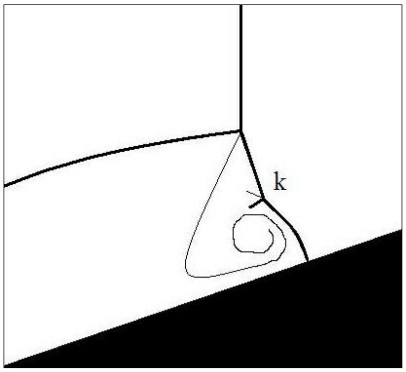

**Figure 3: Sketch of bifurcating Mach reflection. The new triple point that forms is labelled k.**

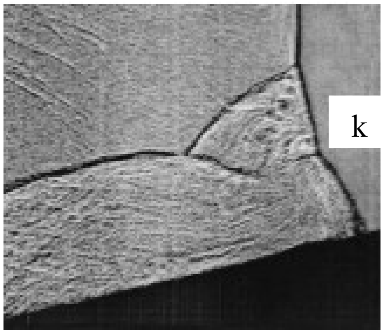

**Figure 4: Shadowgraph of a bifurcating Mach shock reflection in $CCl_2F_2$, with $M_s$=4.94, and $\theta_w$=15°. Taken from Semenov et al. (2009).**

## 1.2 Detonations

Shock reflections are present at the front of detonation waves. A detonation wave is a supersonic combustion wave; it consists of a shock wave that is supported by an exothermic reaction. However, detonation waves have been experimentally observed to be unstable (White (1961) was the first to make this observation). The detonation front thus consists of multiple shock segments which meet at triple points, and these triple points interact and reflect off of each other. A 2D schematic of the detonation structure is shown in Figure 5, illustrating how the triple points interact and reflect off of each other as the detonation moves from left to right. The triple point paths, which are shown with a dashed line in Figure 5, form what is called a cellular structure, and this cellular structure can be captured experimentally with a soot foil.

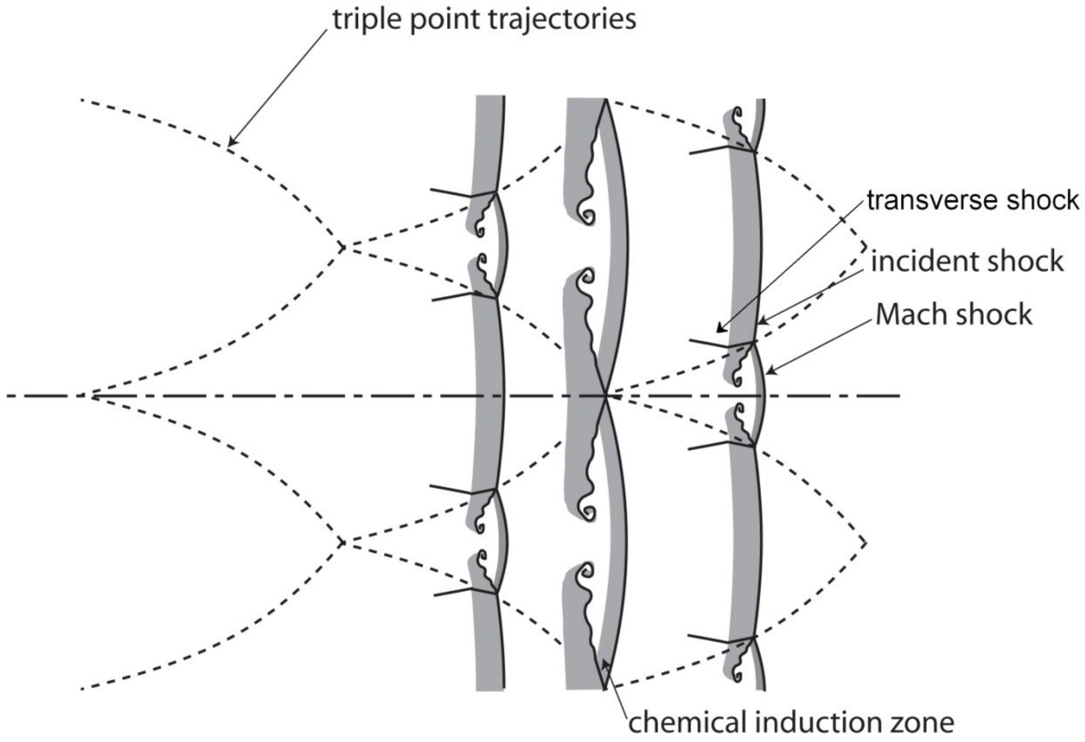

**Figure 5: Schematic of detonation structure. The detonation is moving from left to right. The shock front at three successive times is shown, as well as the triple point paths which form the cellular structure.**

The cellular structure of detonations can range from very regular, to highly irregular, as is shown in Figure 6. Detonations are often classified by the regularity of this cellular structure because regular mixtures behave differently than irregular mixtures. Irregular mixtures are characterized by the constant appearance and disappearance of transverse waves (i.e. triple points), and have been observed to have a much more turbulent reaction zone than regular mixtures (Shepherd 2009). Irregular mixtures have also been found to be less prone to attenuation by boundary losses, or more easily initiated (Radulescu and Lee 2002). In other words, irregular mixtures are more easily detonated. Irregularity has been correlated with high reaction rate sensitivity to temperature perturbations ((Manzhalei 1977), (Austin 2003), (Radulescu 2003)). Therefore, it is believed that irregularity is a result of the instability due to the coupling of the hydrodynamics with the exothermic energy release.

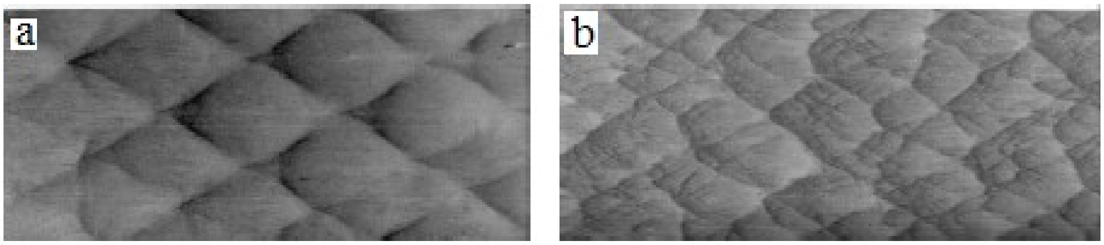

**Figure 6: Soot foils of a) a regular cellular structure ($2H_2$-$O_2$-17Ar, $P_1$=20kPa) and b) an irregular cellular structure ($C_3H_8$-$5O_2$-$9N_2$, $P_1$=20kPa). Taken from Austin (2003).**

Recent numerical simulations of irregular detonations with sufficiently high resolutions ((Sharpe 2001), (Deiterding 2003), (Radulescu, Sharpe, et al. 2007)) showed bifurcations of the Mach stem immediately after a triple point collides either with a wall or another triple point. However, bifurcations have not been observed in numerical simulations of regular detonations ((Deiterding 2003), (Hu, et al. 2004), (Liang, et al. 2007)). An example of a bifurcation occurring in a numerical simulation of an irregular detonation is shown in Figure 7, where a new triple point, labelled *k*, is formed after the triple point reflects off the lower wall. The vortex directly behind the new triple point is identical to the one observed in bifurcating inert shock reflection simulations (see Figure 3). Due to the unsteady, small scale nature of cellular detonations, and the limitations of experimental diagnostics, bifurcations have yet to be clearly observed in detonation experiments to the best of our knowledge.

It is likely that these bifurcations are caused by the inert shock reflection phenomenon, and contribute to irregularity since they are a source of new triple points. Thus, the second part of this thesis will investigate whether bifurcations observed in numerical simulations of detonations are caused by the inert shock reflection process.

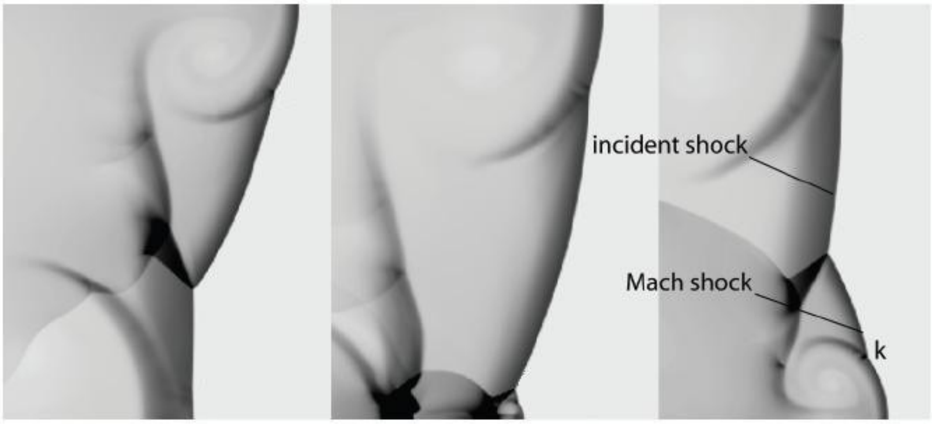

**Figure 7: Three consecutive density plots of a numerical simulation of a detonation ($\gamma$=1.2, $Q/RT_0$=50, and $Ea/RT_0$=27). A bifurcation (labelled k) can be observed after the triple point reflects off the lower wall. Taken from Radulescu (2007).**

## 1.3 Thesis outline

As was previously mentioned, Part 1 of this study is dedicated to determining when these bifurcations occur in inert shock reflections. Relevant background information on inert shock reflections is presented in Section 2.1. To determine when bifurcations occur, systematic numerical simulations across a range of the shock reflection parameters were conducted. The numerical details are given in Section 2.2. Section 2.3 provides the validation of the mathematical model, Section 2.4 provides the results of the simulations, and Section 2.5 provides the results of a resolution and solver study which served to verify the numerical method. Section 2.6 provides the discussion which focuses on an analysis of the shock reflection process aimed to identify the physics controlling the bifurcating regime, as well as the differences expected between the numerical results and real shock reflections.

Part 2 of this study is focused on investigating whether the inert shock reflection phenomenon is the cause of bifurcations observed in irregular detonation simulations. Therefore, a model of the triple point reflection process as an inert shock reflection is proposed in Section 3.1. By doing a thorough validation of the model against cellular detonation simulations, it can be concluded whether the inert shock reflection phenomenon is the cause of the bifurcations in detonations. This validation is presented in Section 3.2. A discussion, which focuses on the effects of these bifurcations on irregularity, is presented in Section 3.3. The conclusions for the entire thesis (both parts) are presented in Section 4.

# 2 Part 1: Bifurcations in shock reflections

## 2.1 Review of Inert Shock reflections

The shock reflection phenomenon is relatively well understood, and has been studied extensively in the past. A review of the findings relevant to this thesis is presented here.

### 2.1.1 Pseudosteady flow

A shock wave moving at a constant velocity is an example of a pseudosteady flow. This is because the flow is steady in the shock frame of reference, and thus can be analyzed by using steady flow theories. The transformation of the frame of reference from the laboratory frame (where velocities are denoted with a $u$) to the shock frame (where velocities are denoted with a $v$) is called a Galilean transformation, and is shown in Figure 8.

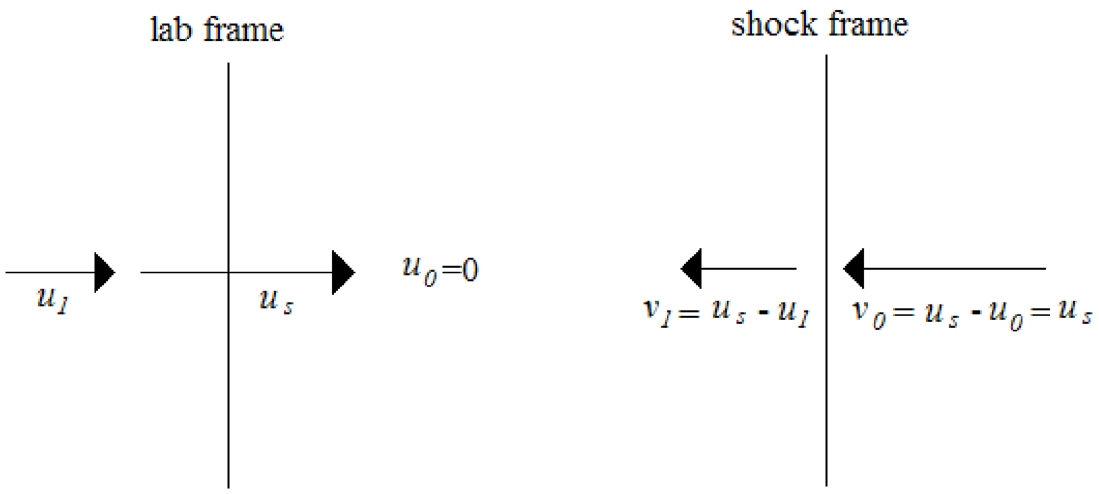

**Figure 8: Galilean transformation.**

Experimental observations of shock reflections conducted in the past (Smith 1945) show that the reflection configuration at a later time is simply a scaled up version of the reflection configuration at an earlier time. That is to say, the shock reflection phenomenon is self-similar. For a Mach reflection, this means that the triple point has a steady trajectory angle, $\chi$, as is demonstrated in Figure 9. The self-similarity of shock reflections indicates that in the frame of reference attached to where shocks intersect, the flow is steady. In other words, shock reflections are an example of a pseudosteady flow. A Mach reflection can thus be analyzed with steady flow theories by attaching a frame of reference to the triple point.

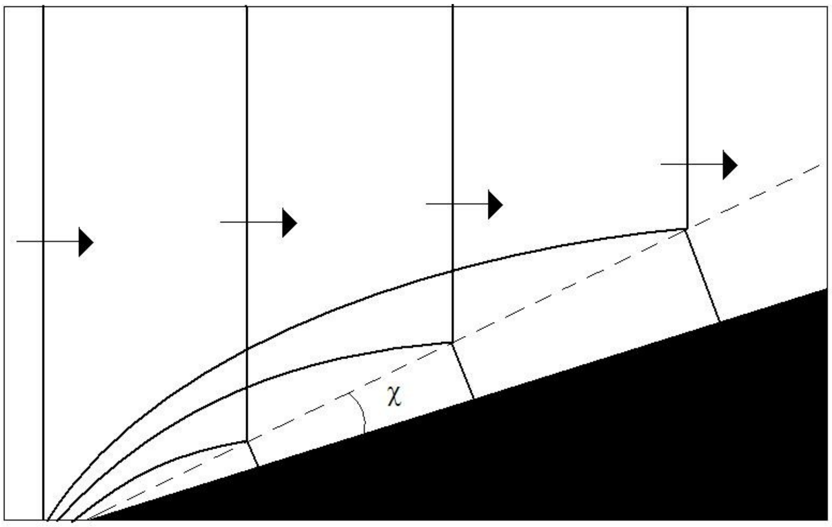

**Figure 9: Schematic of a Mach reflection at various times demonstrating self-similarity and the associated steady trajectory angle, $\chi$.**

### 2.1.2 Analytical approach for Mach reflections

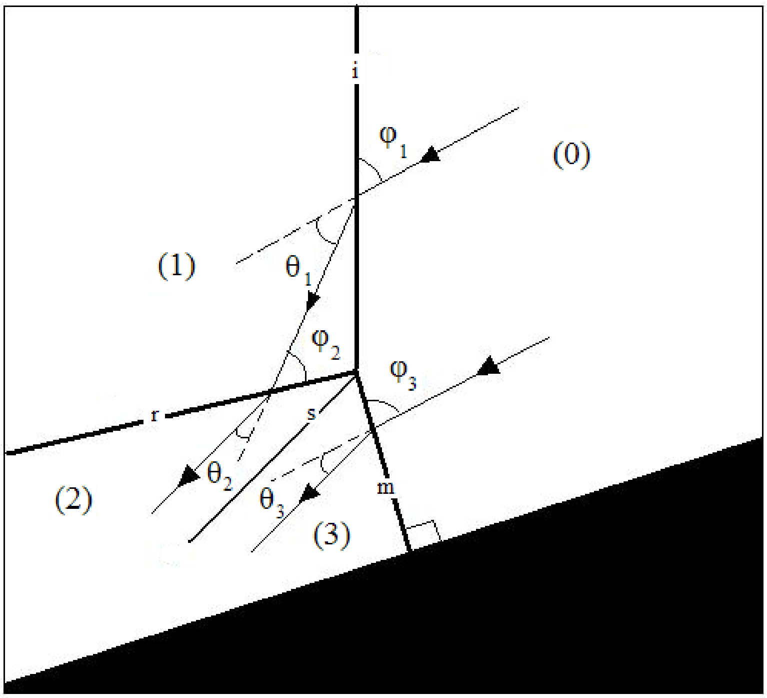

**Figure 10: Mach reflection with frame of reference attached to the triple point. The flow is incident on each shock at some angle $\varphi$, and gets deflected by an angle $\theta$.**

As was discussed in Section 2.1.1, it is possible to analyze a Mach reflection with steady flow theories by attaching a frame of reference to the triple point because of the experimentally observed self-similarity. In this frame reference, the flow is incident on each shock at some angle $\varphi$, and gets deflected by an angle $\theta$, as shown in Figure 10. Oblique shock jump relations derived based on assuming an inviscid, non-heat conducting, perfect gas (see Thompson (1972)) are used to determine the state of the flow behind each shock (e.g. pressure and velocity), as well as the deflection angle. It is thus assumed that viscosity, heat transfer, and real gas effects have a negligible impact on the Mach reflection configuration. The oblique shock jump relations that are relevant to the Mach reflection analysis are shown below (Ben-Dor (2007)).

$$p_j = p_k \frac{2\gamma\left(M_k \sin\phi_j\right)^2 - (\gamma - 1)}{\gamma + 1} \tag{1}$$

$$\theta_j = \tan^{-1}\left[2\cot\phi_j \frac{\left(M_k \sin\phi_j\right)^2 - 1}{{M_k}^2\left(\gamma + \cos 2\phi_j\right) + 2}\right] \tag{2}$$

$$M_j = \csc\left(\phi_j - \theta_j\right)\left[\frac{\gamma + 1 + (\gamma - 1)\left[\left(M_k \sin\phi_j\right)^2 - 1\right]}{\gamma + 1 + 2\gamma\left[\left(M_k \sin\phi_j\right)^2 - 1\right]}\right]^{1/2} \tag{3}$$

where subscripts $k$ and $j$ indicate flow states ahead and behind the shock, $\gamma$ is the ratio of specific heats of the gas, $M$ is the flow Mach number, $\varphi_j$ is its angle of incidence, $\theta_j$ is its deflection angle and $p$ is the pressure. In addition to the oblique shock jump conditions which apply to all three shocks, the flow deflection and the pressure must be the same on both sides of the slipstream. This gives us two additional conditions:

$$\theta_1 - \theta_2 = \theta_3 \tag{4}$$

$$p_2 = p_3 \tag{5}$$

The use of the oblique shock relations and the two matching condition across the slipstream (Equations (1)- (5)) applies to all three shock structures (including detonation triple points), and thus is known as the "three shock theory". Based on geometric considerations, the following two relations can be obtained for the specific case of Mach reflections:

$$\phi_1 = 90° - (\theta_w + \chi) \tag{6}$$

$$M_0 = \frac{M_s}{\sin \phi_1} \tag{7}$$

where $M_s$ is the Mach number of the incident shock in the laboratory frame, $\theta_w$ is the wedge angle, and $\chi$ is the triple point trajectory angle. However, one more relation is needed to close the system of equations: The Mach stem is assumed to be perpendicular to the wedge, and straight, as was first suggested by Law and Glass (1971):

$$\phi_3 = 90° - \chi \tag{8}$$

This assumption appears to be valid since the Mach stem has been experimentally observed to be straight and perpendicular to the wedge under most conditions; in fact, the base of the Mach stem must be perpendicular to the wedge because this ensures that the flow in region 3 (see Figure 10) near the wall is parallel to the wall. The fact that the Mach stem is observed to be straight indicates that the flow in region 3 is uniform.

In order to fully understand the analytical approach, a summary of an iterative solution procedure is given:

1. A particular case of shock reflection is specified by assigning $M_s$, $\theta_w$, and $\gamma$
2. An initial value for $\chi$ must be guessed

3. $\varphi_1$ and $M_0$ can be obtained by using Equations (6), and (7). $p_1$, $\theta_1$, and $M_s$ can then be obtained by using Equations (1), (2), and (3) with $j$=1, $k$=0
4. $\varphi_3$ can be obtained by using Equation (8). $p_3$, and $\theta_3$ can then be obtained by using Equations (1), and (2) with $j$=3, $k$=0
5. $\theta_2$ can be obtained by using Equation (4). $\varphi_2$, and $p_2$ can then be obtained by using Equations (1), and (2) with $j$=2, $k$=1
6. If Equation (5) is satisfied, the solution is achieved. If not, $\chi$ must be adjusted, and we must return to step 2.

A graphical solution is also possible through the use of shock polars (see Law and Glass (1971)). It is important to remember that the velocities obtained in this analysis apply to the triple point frame of reference. To get the velocities in the lab frame of reference, a Galilean transformation must be performed.

### 2.1.3 The entire shock reflection process

As Law and Glass (1971) demonstrated, the entire shock reflection process is actually a combination of two processes: the shock reflection process occurring at the front and the flow deflection process occurring at the back. To understand this, imagine a moving shock that is just about to be reflected by a wedge with the gas particles ahead of the shock coloured white, and the gas particles behind the shock coloured grey, as shown in Figure 11a. The grey particles will be deflected by the wedge in the back, while the white particles will be affected by the shock reflection in the front. In the laboratory frame of reference, the grey particles are moving at a velocity $u_1$, and the shock is moving at a velocity $u_s$. It is clear from the Galilean transformation discussed in Section 2.1.1 that $u_1$ is smaller than $u_s$. This means that at a later time, the flow field behind the incident shock consists of both grey particles, and white particles, as shown in Figure 11b. In other words, the solution of the entire shock reflection flow field comes from the solution of the trailing flow being deflected by the ramp, and the solution of the leading shock reflecting off the ramp. These solutions must merge smoothly together (i.e. no pressure discontinuity)

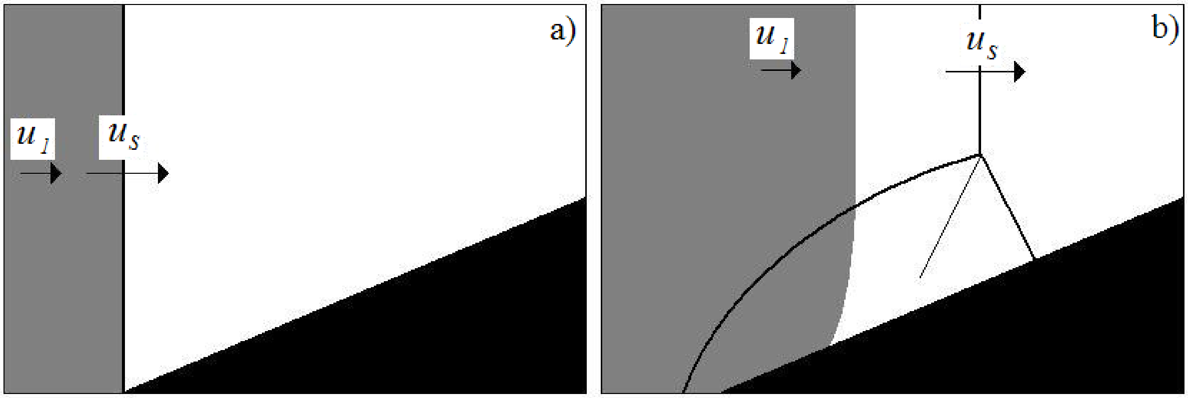

**Figure 11: Sketch of a moving shock a) just about to be reflected by a wedge and b) after reflection.**

This means that the analytical approach presented in Section 2.1.2 only yields part of the entire shock reflection solution. To obtain the full solution, the flow deflection process occurring in the back would have to be considered. In some cases, the flow deflection is simply accomplished with an oblique shock, and thus the flow field can be easily obtained. However, in many cases, the ramp angle $\theta_w$ is so large that the shock is detached. The flow field is thus nonuniform, which means that the flow field can only be obtained via a detailed solution of the equations of motion (i.e. numerical solution). Moreover, the flow deflection solution must merge with the shock wave reflection solution occurring at the front. This means that the flow field in this merging zone will also be nonuniform, and thus can only be obtained via a detailed solution of the equations of motion. In other words, the full flow field of a shock reflection cannot be obtained with a simple analytical approach; a numerical approach is required to obtain the full flow field.

### 2.1.4 Types of Mach reflection

As was highlighted in the previous section, the entire shock reflection process is quite complex; it consists of the merging of the trailing flow deflection process with the lead shock reflection process. It is thus not surprising that three distinct types of Mach reflections have been observed experimentally. A summary of these different configurations is presented here (a more detailed discussion of these configurations can be found in Ben-Dor (2007)).

#### *2.1.4.1 Single Mach reflection*

A single Mach reflection (Figure 12) is characterized by a reflected shock which is curved along its entire length. It tends to occur at low ramps angles and low incident shock Mach numbers.

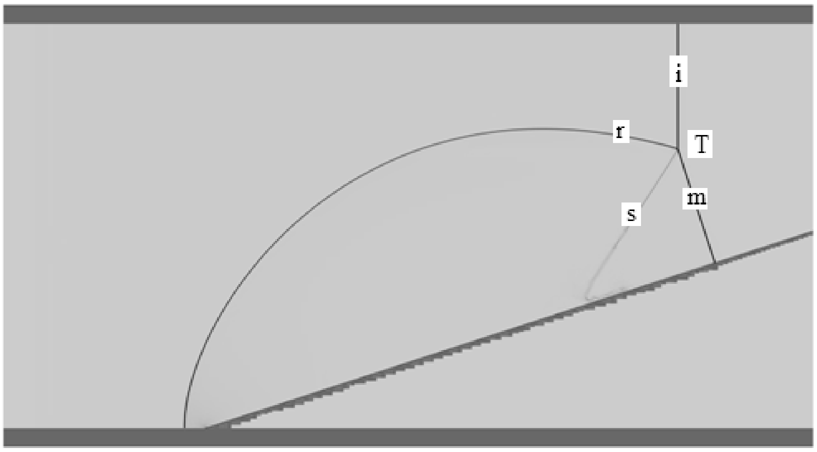

**Figure 12: Schlieren image (i.e. grayscale plot of the gradient of density) obtained from a numerical simulation conducted with $M_s$=2, $\theta_w$=18°, and $\gamma$=1.2 showing a single Mach reflection configuration.**

#### *2.1.4.2 Transitional Mach reflection*

At higher ramp angles and incident shock Mach numbers, the reflected shock develops a kink, and this configuration is known as a transitional Mach reflection (Figure 13). This kink develops when the flow deflection process can no longer communicate with the shock reflection process. This occurs when the flow in region 2 (see Figure 10) becomes supersonic with respect to the triple point

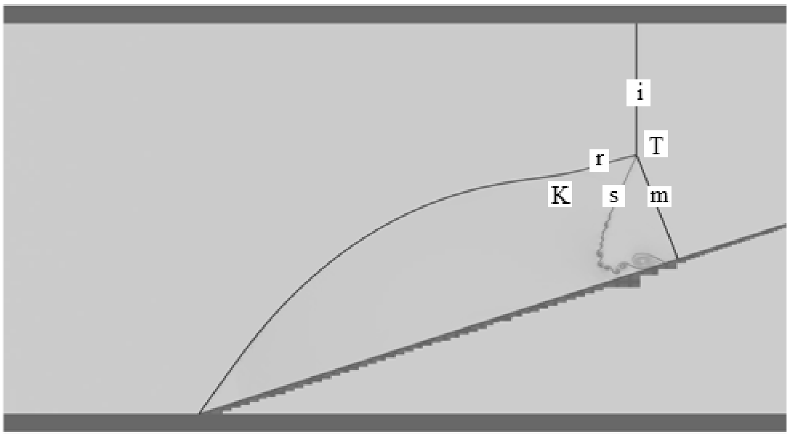

**Figure 13: Schlieren image obtained from a numerical simulation conducted with $M_s$=3, $\theta_w$=18°, and $\gamma$=1.2 showing a transitional Mach reflection configuration. The kink that distinguishes it is labelled K.**

### 2.1.4.3 *Double Mach reflection*

At even higher ramp angles and Mach numbers, the kink becomes a new triple point, and this configuration is known as a double Mach reflection (Figure 14). This new triple point develops when the flow in region 2 (see Figure 10) becomes supersonic with respect to the kink. The slip line associated with the second triple point is difficult to see in a Schlieren image because the shocks connected to that triple point are weak, and thus the density difference (or gradient) between the fluid that is processed by two shocks and the fluid that is processed by one shock is small.

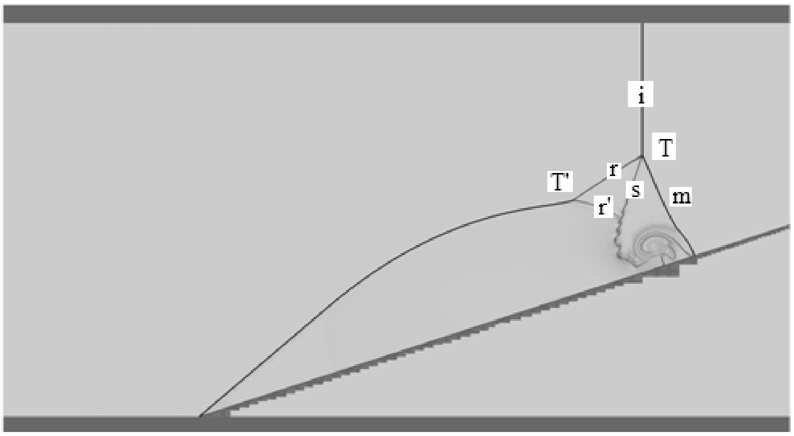

**Figure 14: Schlieren image obtained from a numerical simulation conducted with $M_s$=5, $\theta_w$=18°, and $\gamma$=1.2 showing a double Mach reflection configuration. The second triple point and additional shock that distinguish it are labelled T' and r' respectively.**

## 2.2 Numerical details

As was mentioned in Section 2.1.2, a numerical approach must be used in order to solve the entire flow field resulting from a shock reflection. Thus, in this study we used numerical simulations to determine the conditions for which bifurcations occur.

The entire shock reflection flow field is assumed to be well captured by the Euler equations for a perfect gas with constant specific heats and molecular weight:

$$\frac{D\rho}{Dt} + \rho\nabla \cdot U = 0;\ \ \rho\frac{DU}{Dt} + \nabla p = 0;\ \ \rho\frac{De}{Dt} = \frac{p}{\rho}\frac{D\rho}{Dt}$$

where $D/Dt$ denotes the material derivative $D/Dt \equiv \partial/\partial t + U \cdot \nabla$, and $U$ denotes the velocity vector. The internal energy is given by $e = RT/(\gamma - 1)$, where the temperature can be found from the ideal gas law, $p = \rho RT$.

The simulations were conducted on a domain that had 128 base grid points in the $x$ direction by 64 base grid points in the $y$ direction. The base of the ramp was positioned at the 32nd base grid point in the $x$ direction. Reflective boundary conditions were imposed on the top and bottom boundaries. The shock wave was initiated by imposing the shock jump relations for a calorically perfect gas at the 16th base grid point in the $x$ direction.

The model detailed above was solved with the AMRITA CFD package developed by Quirk (1998). The ramp was created by using the embedded boundary technique and applying the level-set method developed by Xu et al. (1997). The Roe approximate Riemann solver (Roe 1981) was used as the solver, unless otherwise specified. The AMRITA environment uses an adapative mesh refinement scheme in order to save computational time. It does this by using a tiered grid system. The maximum number of grids (*lmax*) is set by the user. Each grid can refine the existing grid by the set refinement ratio ($r$). This means that the maximum number of grid points per base grid point is equal to $r^{lmax}$. The default case used in this study was $lmax$=2, and $r$=4 unless otherwise specified. The regions where more grids are to be used can be specified by setting the refinement criteria. In our case, regions with a higher density gradient (i.e. shocks and slip lines) were more refined. The temporal resolution was controlled by the CFL number, which was set to 0.8. The AMRITA script used for the shock reflection simulations is shown in Appendix A.

Since the shock reflection problem depends on $M_s$, $\theta_w$, and $\gamma$, these parameters were varied in the script in order to determine when bifurcations occur. In order to verify the results, a resolution and solver study was conducted. The resolution study was conducted by varying the refinement ratio, $r$, in the script. The solver study was conducted by varying the Riemann solver (either Roe (Roe 1981), Godunov (Godunov 1959), EFM (Pullin 1980), HLLE (Einfeldt 1988), or AUSM (Liou and Steffen 1993)) used in the script.

## 2.3 Model Validation

To ensure that the model discussed above accurately captures the shock reflection phenomenon, a simulation was run and compared to an experiment from Glaz, et al.(1985) (air, $M_s$ =8.7, $\theta_w$ =27°, $p_0$=4.1kPa, and $T_0$=299.2K). The input parameters for the simulation are $M_s$, $\theta_w$, and $\gamma$. Since $\gamma$ in reality is a function of temperature and thus takes on different values before and after a shock, an assumption for $\gamma$ had to be made. The post incident shock $\gamma$ was selected in order to accurately capture the compressibility in the shocked gases. The post shock $\gamma$ was found to be 1.28 with NASA's CEA program (Gordon and McBride 1994). Therefore, the simulation was conducted with $M_s$ =8.7, $\theta_w$ =27°, and $\gamma$ =1.28 as the parameters. The Schlieren image obtained from the simulation, as well as the experimental interferogram taken from Glaz, et al.(1985) are shown in Figure 15.

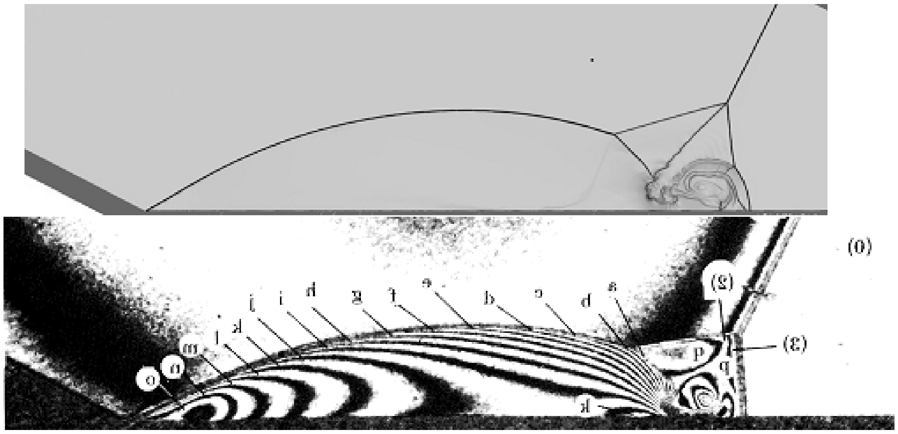

**Figure 15: Schlieren image obtained from numerical simulation ($M_s$ =8.7, $\theta_w$ =27°, and $\gamma$ =1.28) on top, and interferogram obtained from experiment (air, $M_s$ =8.7, $\theta_w$ =27°, $p_0$=4.1kPa, and $T_0$=299.2K) taken from Glaz, et al.(1985) below.**

## 2.4 Results

Results based on the approach discussed in Section 2.2 are presented here. Schlieren images are used to depict the flow fields since Schlieren images are simply a grayscale plot of the density gradient, and thus they expose shock waves and slip lines.

The Schlieren images obtained by varying $M_s$ ( keeping $\theta_w$, and $\gamma$ constant), by varying $\theta_w$ (keeping $M_s$, and $\gamma$ constant), and by varying $\gamma$ ( keeping $M_s$, and $\theta_w$ constant) are presented in Figure 16, Figure 17, and Figure 18 respectively.

Figure 16 shows that when $M_s$ is low ($M_s$=2), a single Mach reflection is observed, when $M_s$ is higher ($M_s$=3), a transitional Mach reflection is observed, and when $M_s$ is even higher ($M_s$=4 and higher), a double Mach reflection is observed. More importantly, as $M_s$ is increased, the slip line vortex becomes larger, and eventually a bifurcation is visible at $M_s$=6.

Figure 17 shows that when $\theta_w$ is low ($\theta_w$=5°), a single Mach reflection is observed, when $\theta_w$ is higher ($\theta_w$=10°), a transitional Mach reflection is observed, when $\theta_w$ is higher than that ($\theta_w$=15-40°), a double Mach reflection is observed, and when $\theta_w$ is further increased ($\theta_w$=45°) a regular reflection is observed. More importantly, as $\theta_w$ is increased, the slip line vortex becomes larger, and eventually a bifurcation is visible at $\theta_w$=20°.

Figure 18 shows that when $\gamma$ is low ($\gamma$=1.1-1.35), a double Mach reflection is observed, and when $\gamma$ is high ($\gamma$=1.4-1.5), a transitional Mach reflection is observed. More importantly, as $\gamma$ is increased, the slip line vortex becomes smaller, and eventually the bifurcation that is visible at low $\gamma$ disappears at $\gamma$=1.25.

It is clear from the results presented above that bifurcations occur as $M_s$ is increased, $\theta_w$ is increased, and $\gamma$ is decreased. It is also clear that as the parameters are changed in favour of bifurcation formation, the slip line first begins to curve forward, the resulting vortex that forms gets bigger and closer to the Mach stem, and eventually a bifurcation forms.

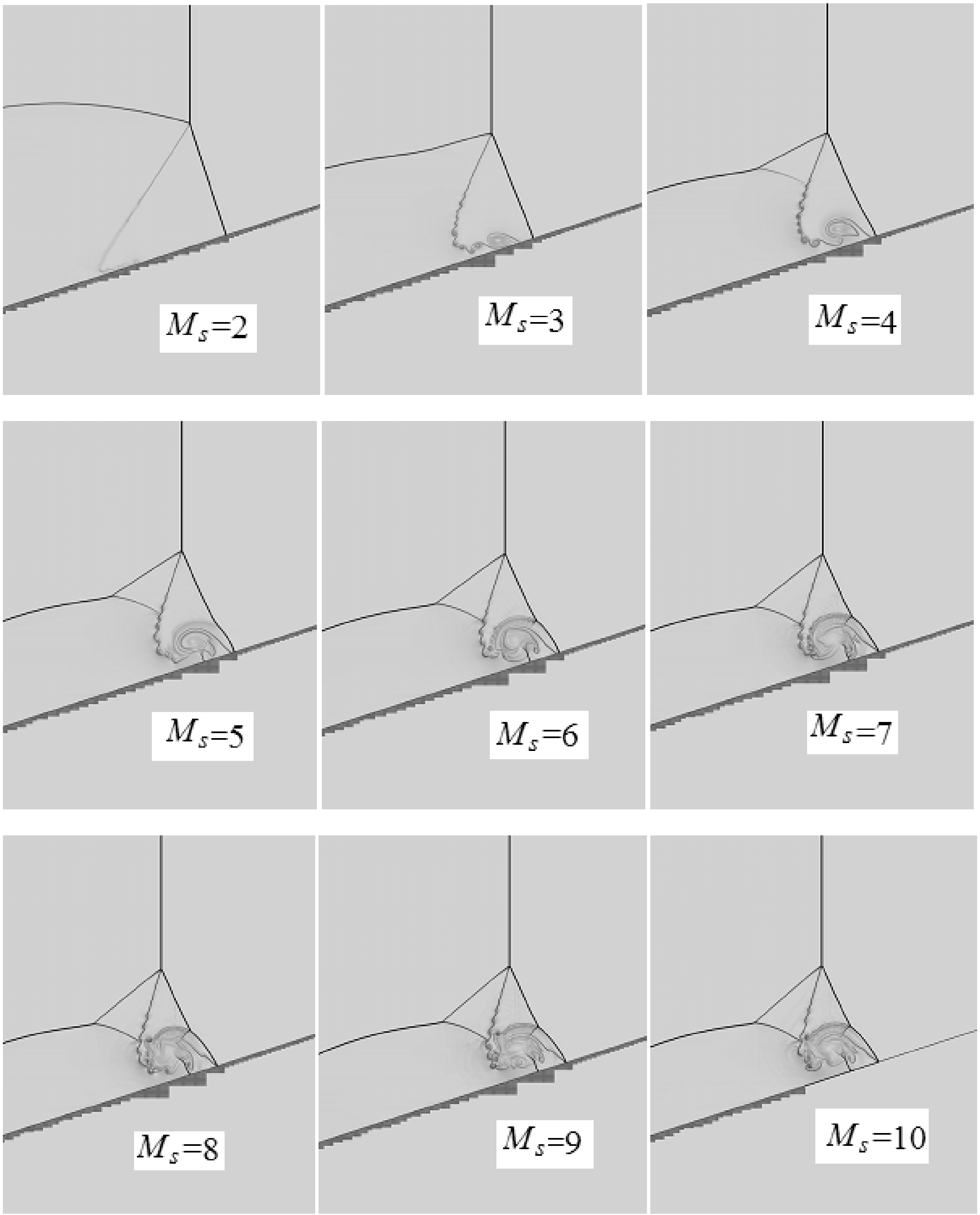

**Figure 16: Schlieren images obtained by varying $M_s$. $\gamma$=1.2, $\theta_w$=18°, and $M_s$ is indicated on the figure. The incident shock is approximately 70 base grid points away from the corner in all images.**

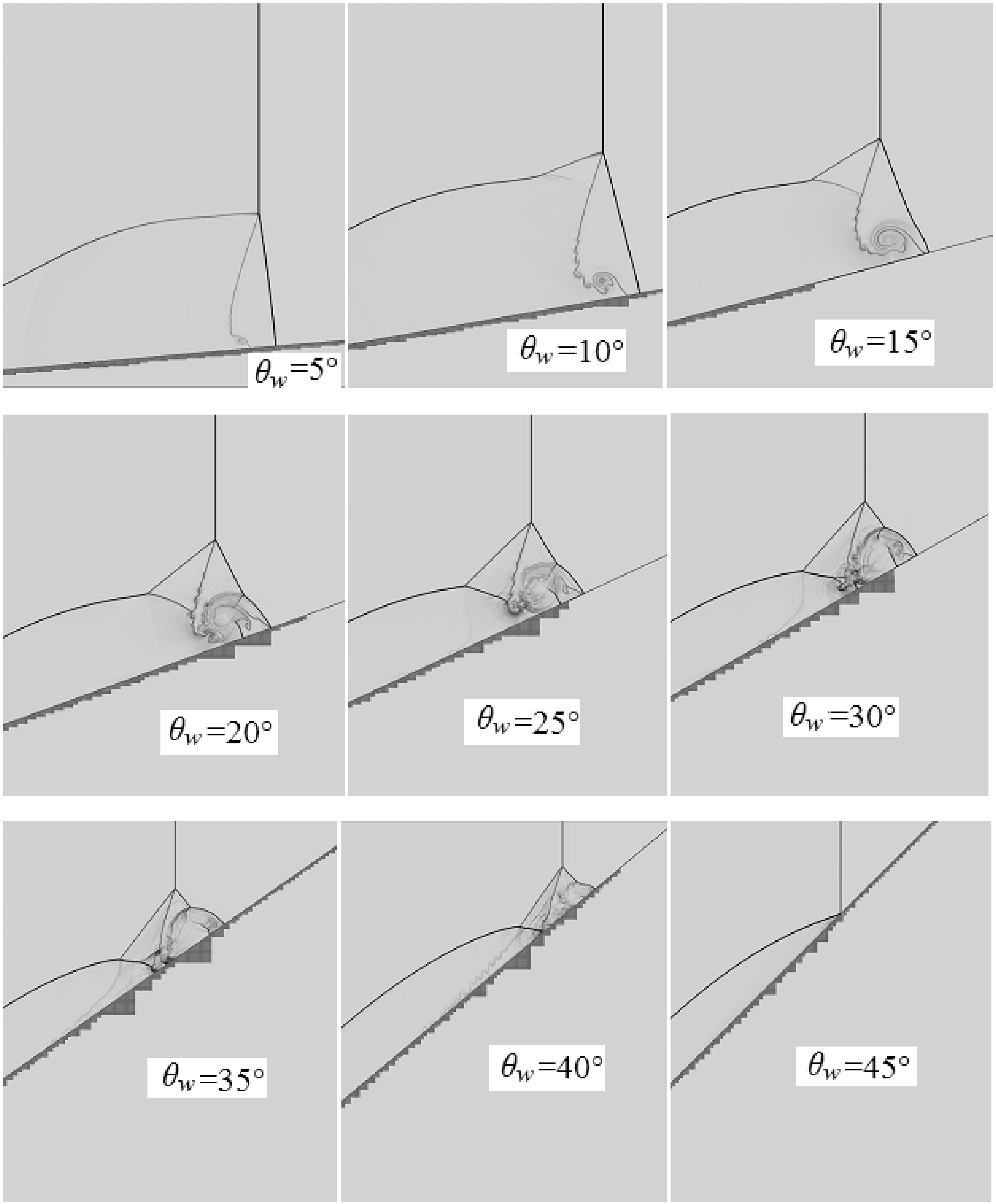

**Figure 17: Schlieren images obtained by varying $\theta_w$. $\gamma$=1.2, $M_s$=6, and $\theta_w$ is indicated on the figure. The incident shock is between 50-85 base grid points away from the corner in all images.**

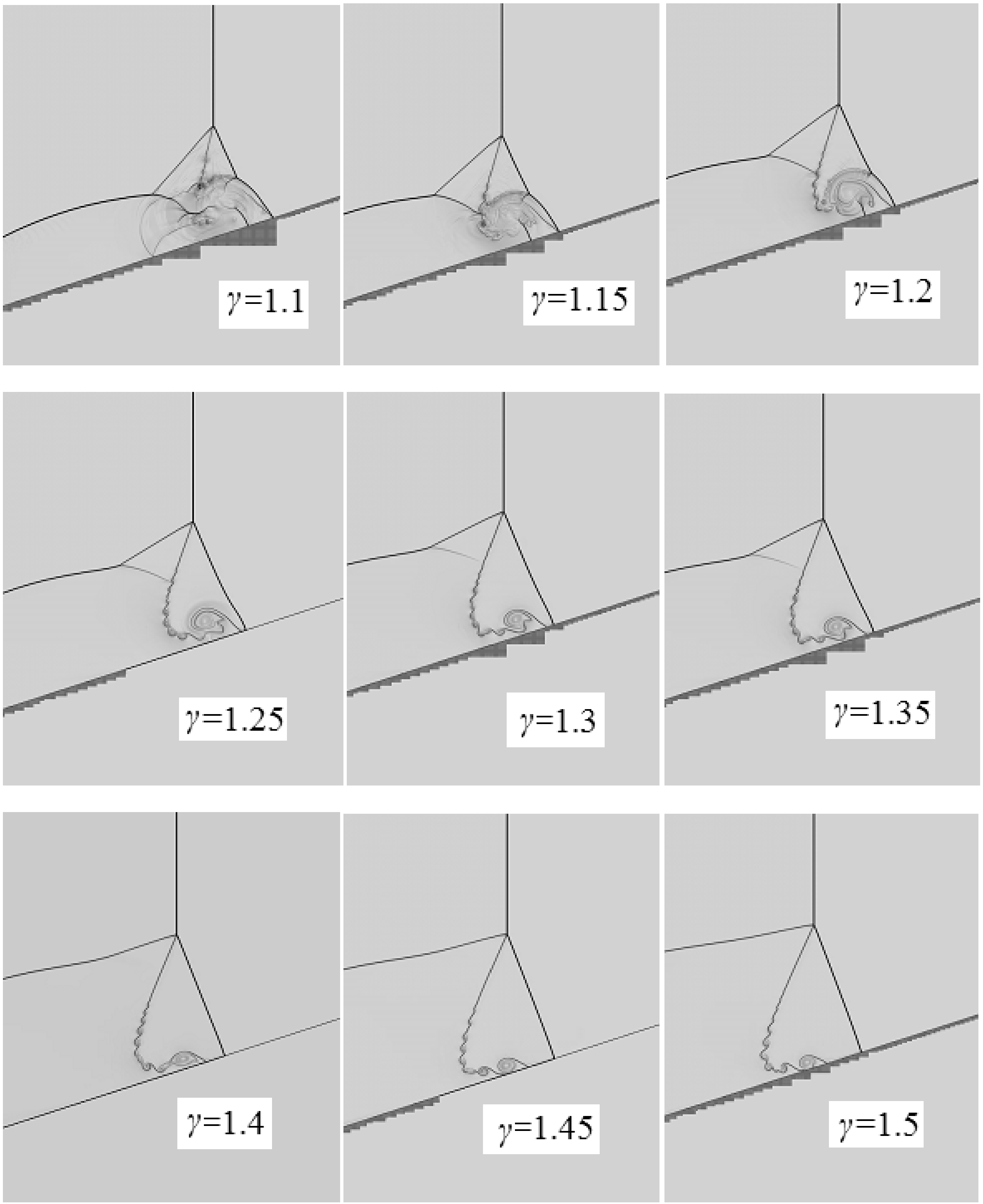

**Figure 18: Schlieren images obtained by varying $\gamma$. $\theta_w$ =18°, $M_s$=6, and $\gamma$ is indicated on the figure. The incident shock is approximately 70 base grid points away from the corner in all images.**

To summarise the results of many inert shock reflection simulations across a wide range of parameters, the bifurcation transition points in the ($M_s$, $\theta_w$)-plane for $\gamma$=1.1, 1.2, 1.3, 1.4, and 1.5 are presented in Figure 19. Lines connect the points to show the bifurcation boundary. The transition points were obtained by setting $\gamma$ and $\theta_w$, and increasing $M_s$ by increments of 1 until a bifurcation was observed (hence the error bars associated with the points).

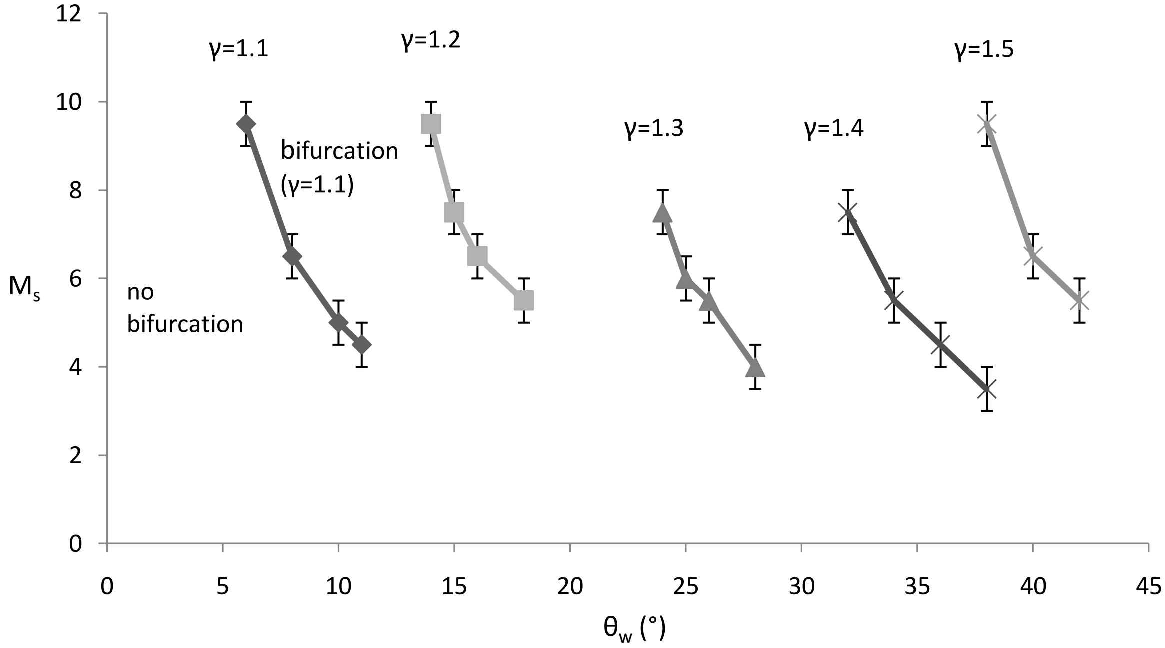

**Figure 19: Bifurcation transition points for $\gamma$=1.1, 1.2, 1.3, 1.4, and 1.5. Lines connect the points to show the bifurcation boundary. Shock reflections with parameters below and to the left of a line did not have bifurcations, while shock reflections with parameters above and to the right of a line did have bifurcations.**

In all the results presented above, bifurcations were only visible in the double Mach reflection regime, which occurs at sufficiently large ramp angles. If the ramp angle is further increased, a regular reflection occurs. Figure 20 shows that bifurcations disappear before a regular reflection occurs. In other words bifurcations appear and disappear within the double Mach reflection regime.

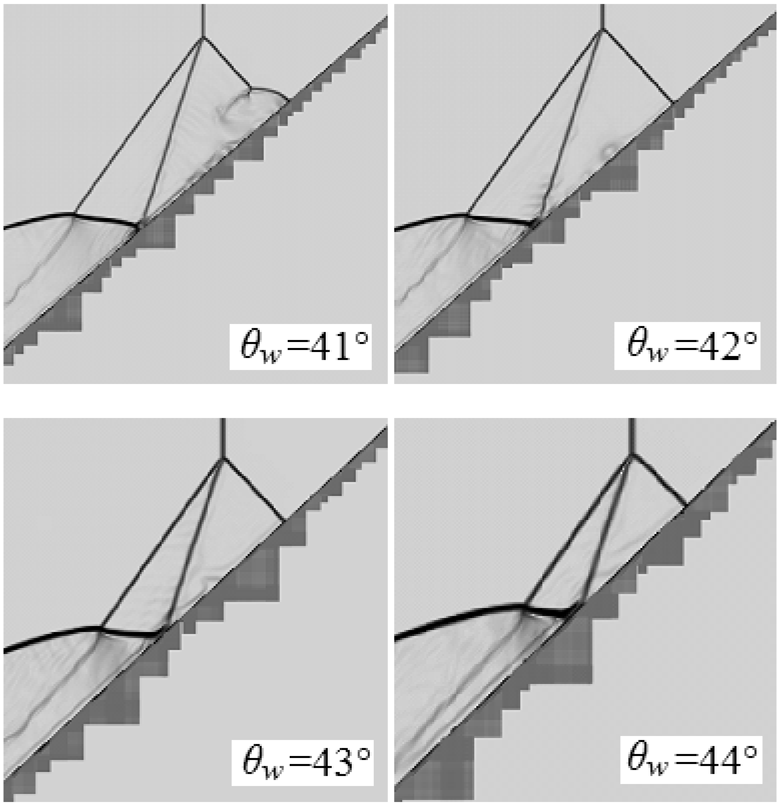

**Figure 20: Schlieren images obtained by varying $\theta_w$. $\gamma$=1.2, $M_s$=6, and $\theta_w$ is indicated on the figure. The incident shock is between 50-60 base grid points away from the corner in all images.**

## 2.5 Verification: Resolution and solver study

In order to verify that the numerical procedure used solves the mathematical model accurately, a resolution and solver study was conducted. The Schlieren images obtained by varying the resolution ( keeping $M_{s,}$ $\theta_w$, and $\gamma$ constant), and by varying the solver (keeping $M_{s,}$ $\theta_w$, and $\gamma$ constant) are presented in Figure 21 and Figure 22 respectively.

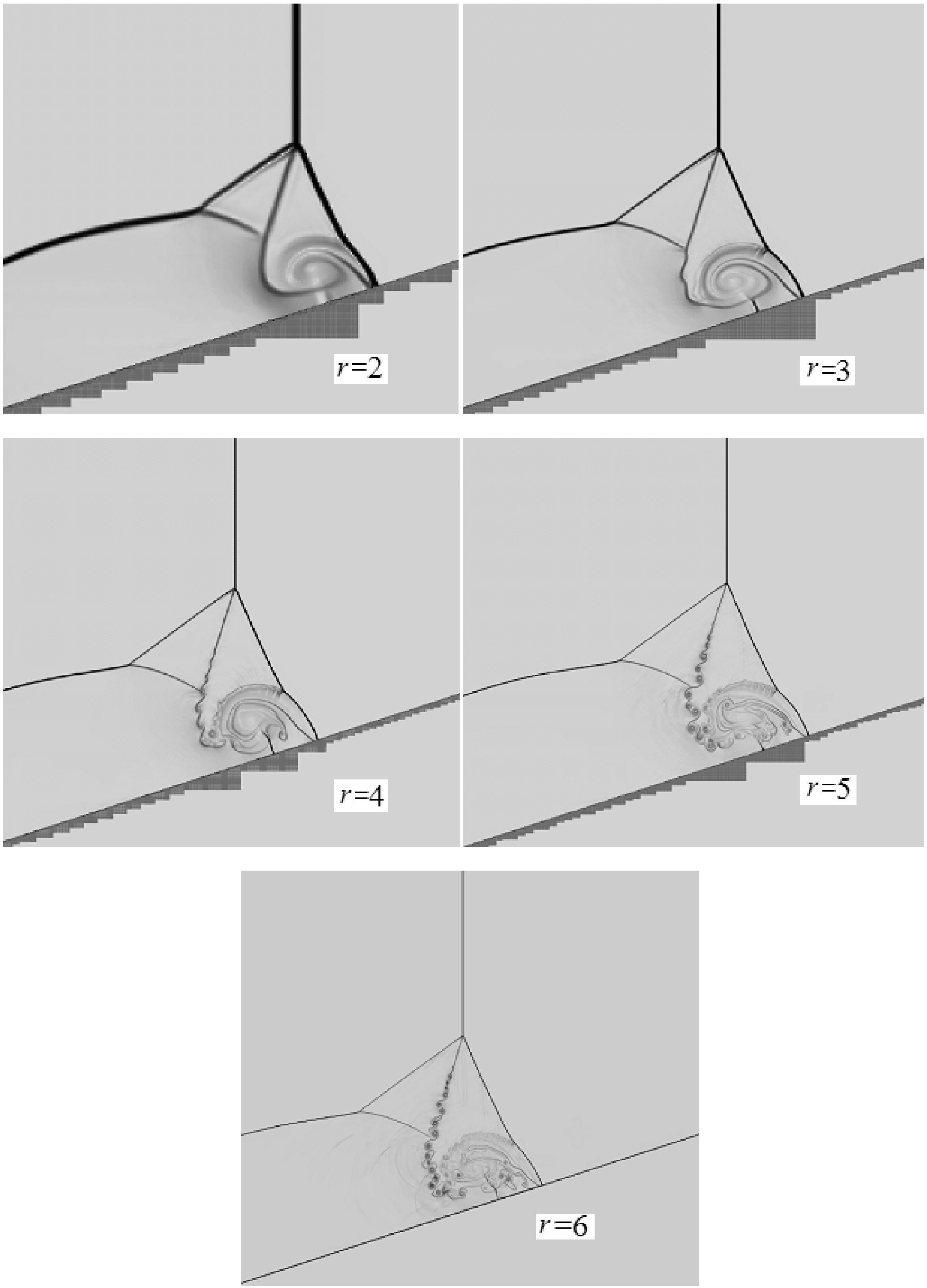

**Figure 21: Schlieren images obtained by varying the refinement ratio, $r$. $\theta_w$=18°, $M_s$=6, $\gamma$=1.2, and $r$ is indicated on the figure. The incident shock is approximately 280, 630, 1120, 1750, and 2520 of the finest grid points away from the corner for the images corresponding to $r$=2, 3, 4, 5, and 6 respectively.**

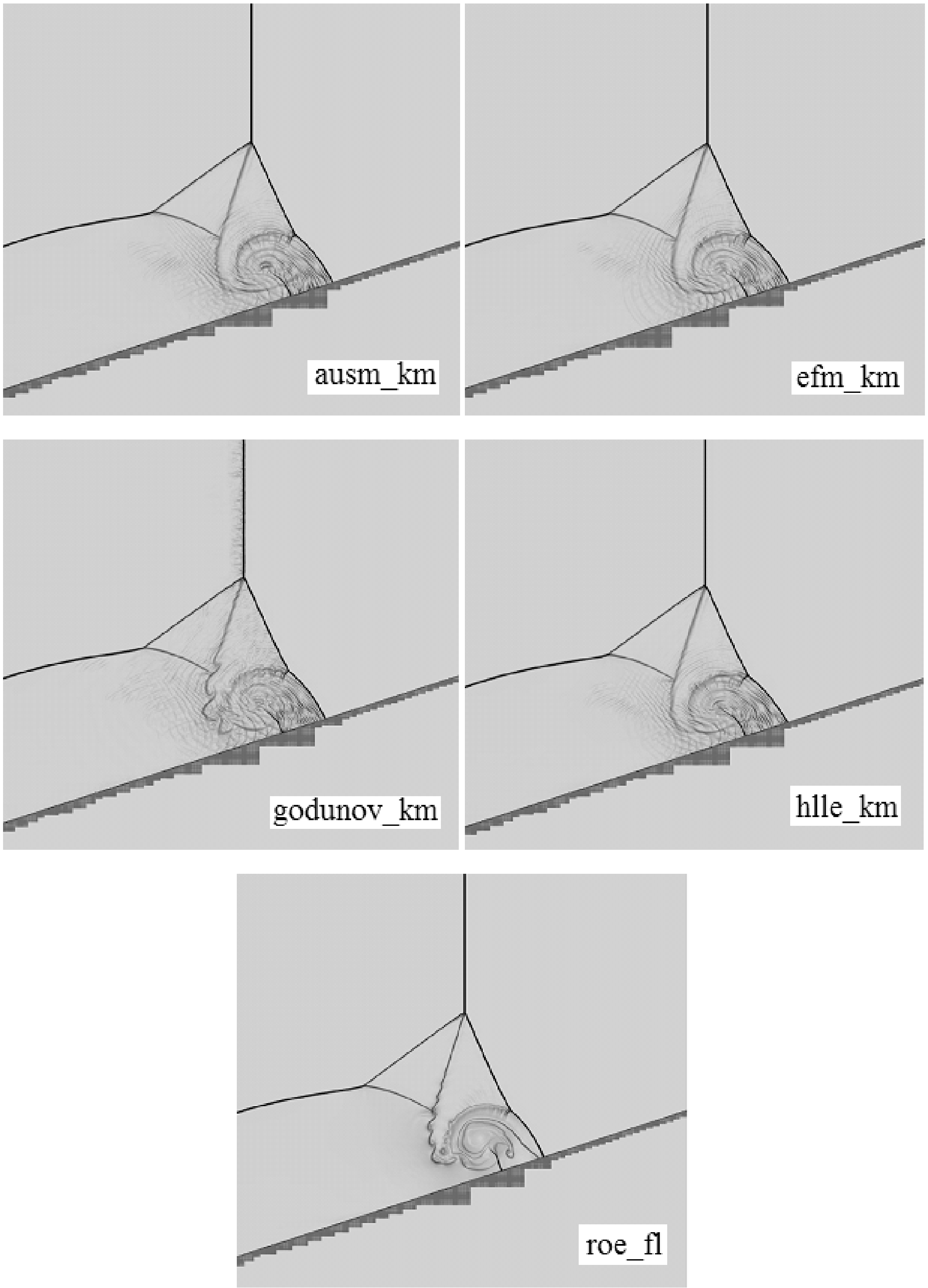

**Figure 22: Schlieren images obtained by varying the solver. $\theta_w$=18°, $M_s$=6, $\gamma$=1.2, and the solver is indicated on the figure. The incident shock is approximately 70 base grid points away from the corner in all images.**

Figure 21 shows that as the resolution is increased from $r = 2$ to $r = 5$, the Mach stem kink becomes more prominent, and bifurcations are observed for $r \geq 3$. The prominence of the kink appears very similar or the $r = 3$, 4, and 5 simulations; however, the Mach stem kink becomes less prominent at $r = 6$. Vortices on the slip line are present and more prominent at higher resolutions. These vortices are a result of Kelvin Helmholtz instability, which is caused by the velocity difference across the slip line.

Figure 22 shows that the various solvers yield very similar results in terms of the prominence of the bifurcation. The Roe solver yields results that are less noisy than the results obtained by the other solvers, and thus it is possible that the type of solver used could have an effect on the bifurcation transition parameters.

To further understand the effects that resolution and type of solver used have on the bifurcation transition parameters, another bifurcation boundary graph is presented in Figure 23. In this figure, bifurcation transition points for $\gamma=1.2$ obtained by using the hlle_km solver (with $r = 4$), and by using $r = 2$ (with the roe_fl solver), are compared to the transition points obtained by using the usual method (roe_fl solver, $r = 4$). Again, the transition points were obtained by setting $\theta_w$, and increasing $M_s$ by one until a bifurcation was observed, and lines connect the points to show the bifurcation boundary.

Figure 23 shows that, although variations to the numerical simulations (either resolution, or solver used) do have an effect on quantitatively predicting bifurcation, they do not have an effect on qualitatively predicting bifurcations; they still occur when $M_s$ is large, $\theta_w$ is large, and $\gamma$ is small.

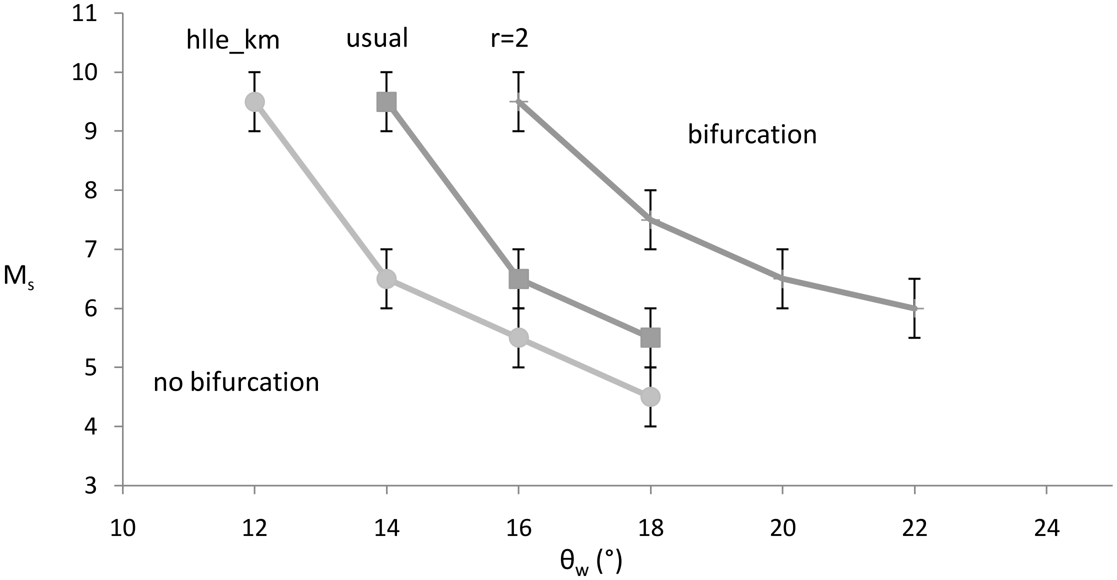

**Figure 23: Bifurcation transition points for *γ*=1.2 obtained by using the hlle_km solver, and with *r*=2. The transition points obtained by using the usual method (roe_fl solver, *r*=4) are also shown. Lines connect the points to show the bifurcation boundary. Shock reflections with parameters below and to the left of a line did not have bifurcations, while shock reflections with parameters above and to the right of a line did have bifurcations.**

## 2.6 Discussion

### 2.6.1 Why the slip line curves forward

It is of interest to know why the slip line curves towards the Mach stem, because without this phenomenon, bifurcations would not occur. An analytical model for the transition from no-jetting (curving away from the Mach stem) to jetting (curving towards the Mach stem) has been proposed by Henderson, et al.(2003), however it relies on results from numerical simulations, and thus the reason why the slip line curves towards the Mach stem is not physically clear. In that study, a number of simulations of shock reflection with $\gamma$=1.4 were conducted, and jetting occurred somewhere between $M_s$=1.5 and $M_s$=2 for ramp angles between 10° and 40°. Hornung (1986) pointed out that the pressure near the wall to the left of the slip line (region 2 in Figure 10) must be higher than the pressure near the wall to the right of the slip line (region 3 Figure 10) in order for the slip line to curve forward, and that this higher pressure corresponds to the stagnation of the flow to the right of the slip line (region 3) with respect to the wall. He also mentioned that this pressure gradient can be so severe that it can cause the Mach stem to bulge. However, reasoning for why the slip line does not curve forward in certain situations was not given. Semenov et al. (1970) hypothesized that the slip line curves forward due to the interference of the flow deflection and shock reflection processes, but concrete proof of this hypothesis was not presented. A discussion of why the slip line curves forward from a consistent point of view which unifies the arguments made in the past with numerical support is thus presented here.

The reason the slip line curves one way or the other can be understood by using the analysis presented in Section 2.1.2. Assuming that the Mach stem is perpendicular to the wall and straight, the flow in region 3 is strictly parallel to the wall in the lab frame of reference. Thus, in a frame of reference attached to where a straight slip line would intersect the wall, labelled B, the velocity in region 3 is zero. Point B is thus moving at a velocity $v_3$ in the triple point frame of reference. Thus, with respect to point B, the velocity in region 2 is equal to $v_2 - v_3$, as shown in Figure 24. Since $v_2$ is always greater than $v_3$ (see Henderson, et al (2003) for explanation), the flow in region 2 has a component perpendicular to the wall. That means that if the slip line was straight, there would be a stagnation point and thus a high pressure just to the left of point B, and the pressure condition across the slip line would not be satisfied. This means that the slip line must bend one way or the other to convert the velocity component perpendicular to the wall in region 2 to a component parallel to the wall.

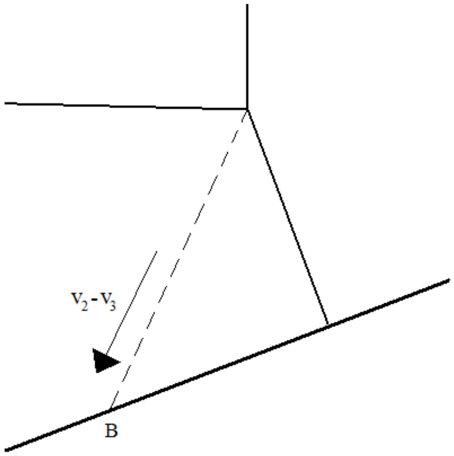

**Figure 24: Diagram showing the velocity of region 2 with respect to point B, the point where an imaginary slip line would intersect the wall. The velocity of region 3 with respect to point B is zero.**

Whether the slip line bends towards the corner or away from the corner depends on the solution (i.e. pressure) of the flow deflection process occurring behind the shock reflection process, as Semenov et al. (1970) pointed out. Let's consider the case where the slip line curves towards the wedge corner and becomes tangent to the wall (see Figure 25). The more the slip line curves towards the corner, the more the velocity in region 3 has to increase (so that fluid fills the entire region) along the slip line. Since the Euler equation along a streamline states that $\frac{1}{\rho}\frac{\partial P}{\partial s} = -v\frac{\partial v}{\partial s}$ (where $s$ is the distance along the streamline), this means that the pressure decreases, and the more the slip line curves, the more the pressure decreases. Since the pressure from the shock reflection solution (white region in Figure 11) must match the pressure from the flow deflection process (grey region in Figure 11), the slip line can only curve to the left if the pressure in the white region is higher than the grey region. The amount of curvature depends on the pressure difference between the two regions.

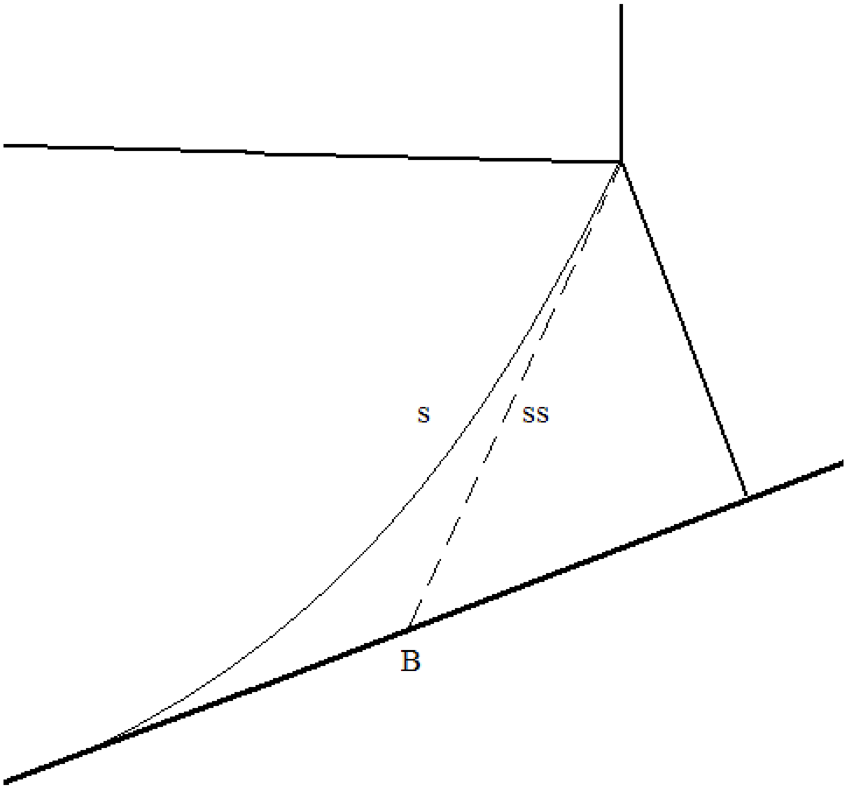

**Figure 25: Diagram of slip line curving towards the wedge corner. The dashed line, labelled ss, represents an imaginary straight slip line for reference purposes.**

Our numerical results showed that the slip line curves towards the wedge corner at low Mach numbers. A Schlieren image obtained for $M_s$=1.5, $\theta_w$=32°, and $\gamma$=1.4, as well as the pressure reading along the wall are shown in Figure 26. It is clear that the pressure corresponding to the flow deflection solution is low, and thus the slip line curves to the left in order to match the two solutions.

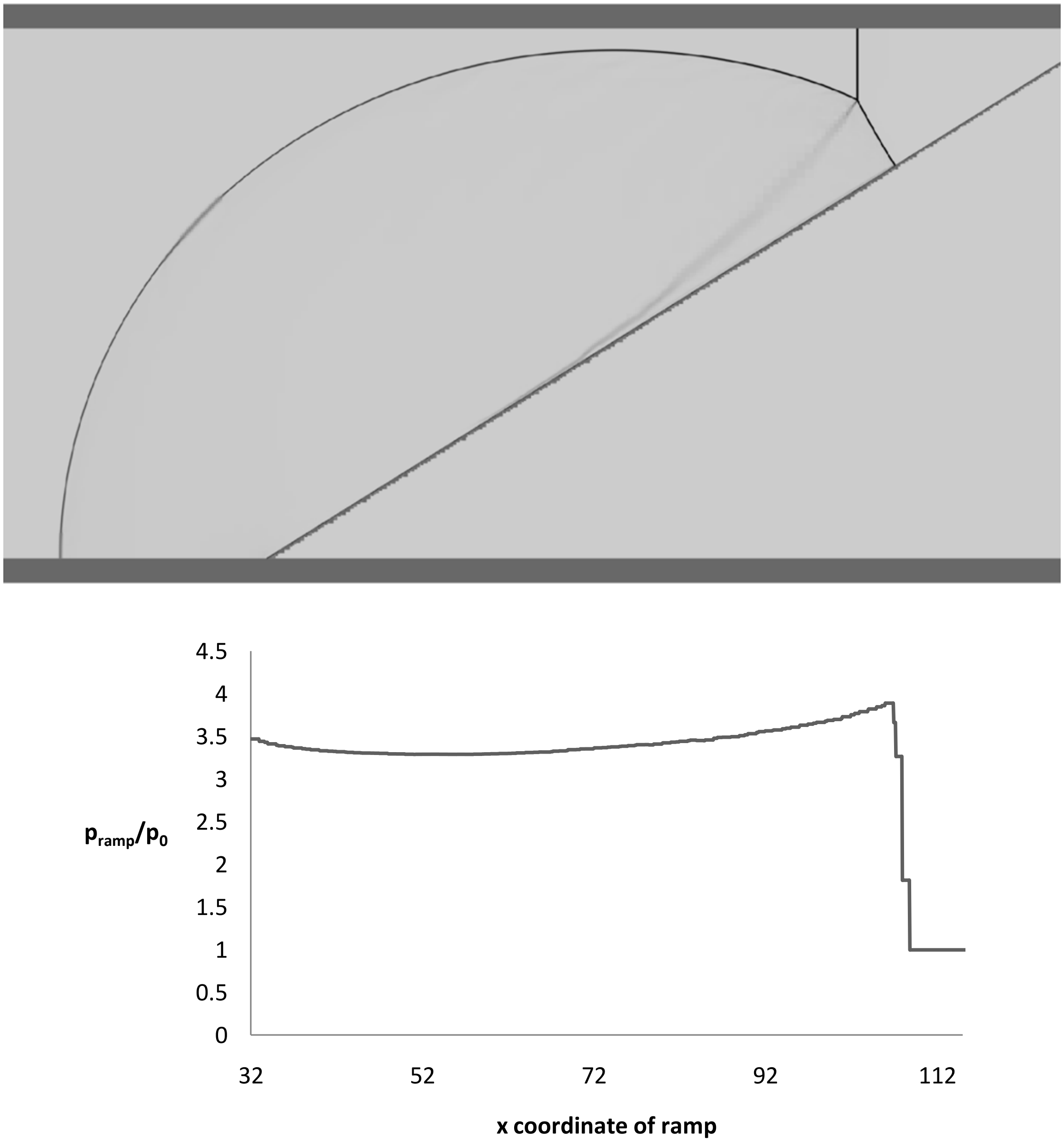

**Figure 26: Schlieren image (above) and a graph of pressure along the ramp, $p_{ramp}$, (below) obtained from a numerical simulation conducted with $M_s$=1.5, $\theta_w$=32°, and $\gamma$=1.4. The Schlieren image shows the slip line curving towards the wedge corner.**

If the pressure is higher in the grey region than the white region, the slip line can no longer curve to the left. Consequently, it must curve to the right, as shown in Figure 27. This means that some of the flow in region 2 must go to the right (which we will call region 4), and the remainder of the flow in region 2 must go to the left. This means that there must be a peak pressure at a certain point diverting the flow. As Hornung (1986) pointed out, this pressure is the stagnation pressure of the flow in region 2 with respect to point B (note, this stagnation point may not correspond to exactly where a straight slip line would intersect the wall, but it will be travelling at roughly the same speed as point B, and thus we call it point B). In other words, it is the pressure obtained from the flow in region 2 colliding with the wall. This increased pressure in the white region allows the pressures in both regions to match.

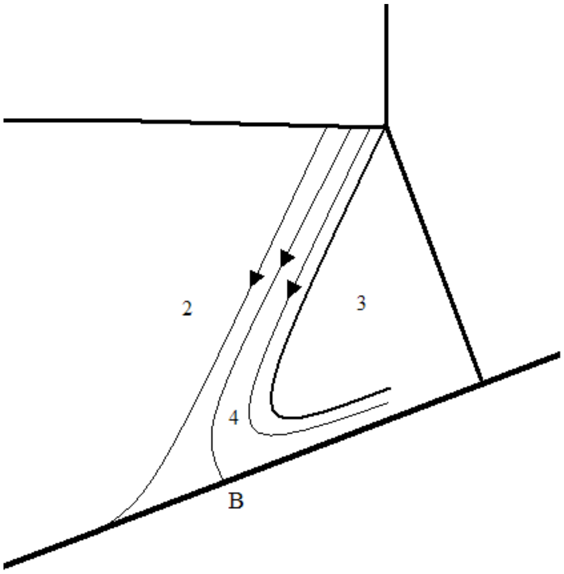

**Figure 27: Diagram of slip line curving towards the Mach stem. Streamlines are drawn with respect to point B.**

Our numerical results showed that the slip line curves towards the Mach stem at high Mach numbers. A Schlieren image obtained for $M_s$=2, $\theta_w$=32°, and $\gamma$=1.4, as well as the pressure reading along the wall are shown in Figure 28. It is clear that the pressure corresponding to the flow deflection solution is high, and thus the slip line curves to the right in order to match the two solutions. Also, a high pressure corresponding to the stagnation streamline is observed in the pressure reading.

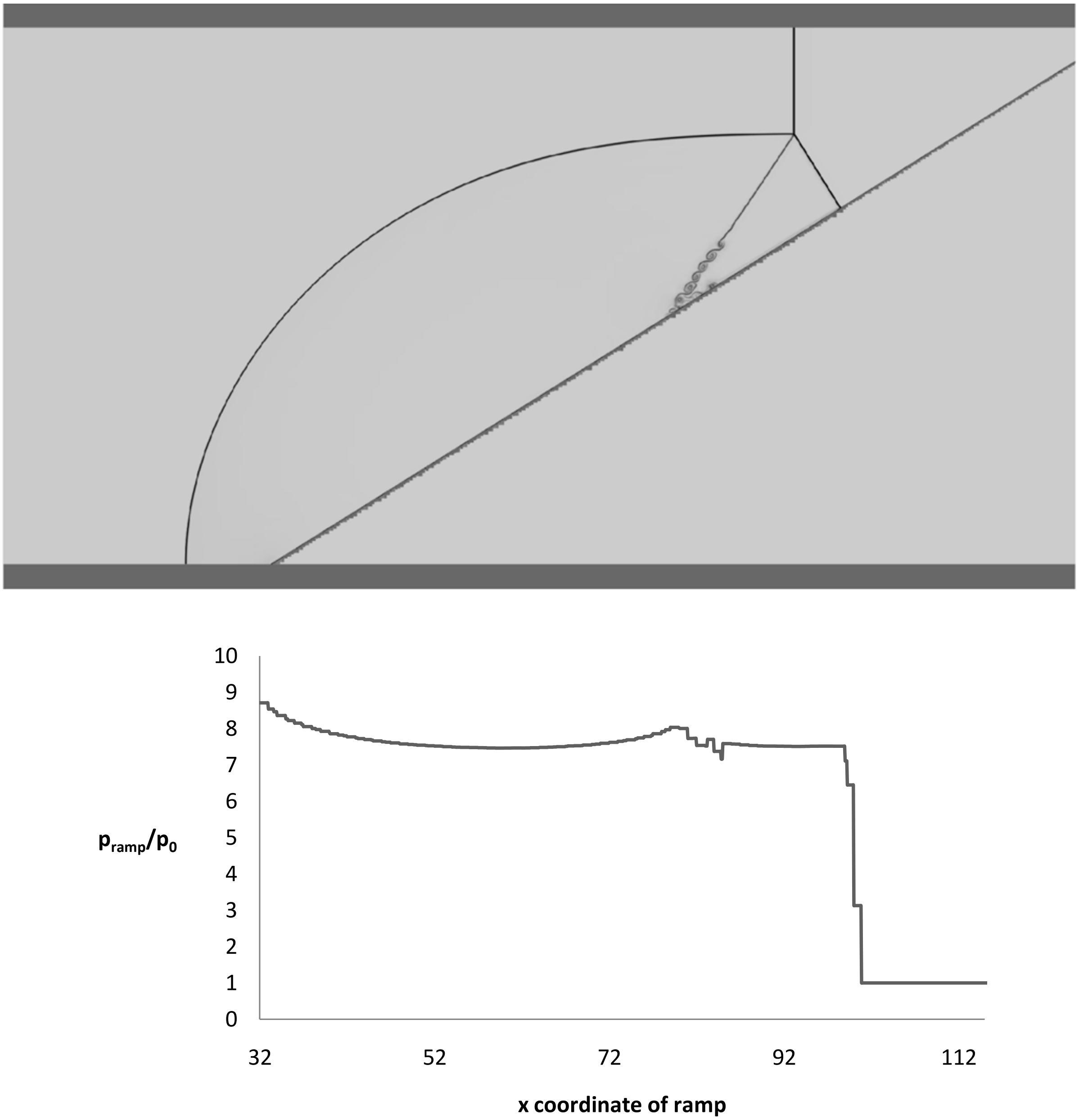

**Figure 28: Schlieren image (above) and a graph of pressure along the ramp, $p_{ramp}$, (below) obtained from a numerical simulation conducted with $M_s$=2, $\theta_w$=32°, and $\gamma$=1.4. The Schlieren image shows the slip line curving towards the Mach stem.**

### 2.6.2 The mechanism of bifurcation formation

As Hornung (1986) pointed out, the pressure at B can be so severe as to drive a wall jet to the right that influences the Mach stem (i.e. bifurcation of the Mach stem). We know based on the above discussion that the pressure is simply a result of the stagnation of the streamline in region 2 at point B, and the velocity of the stagnation streamline with respect to point B is equal to $v_2$ - $v_3$. Consequently, the velocity of the streamlines that jet towards the Mach stem (region 4 in Figure 27) is $v_2$ - $v_3$ with respect to point B (since the pressure across the slip line must match, and thus the velocity of region 4 cannot change). If we assume that a bifurcation of the Mach stem occurs when the jet catches up to the Mach stem, and that the slip line curves forward for Mach numbers greater than 2 (since this is what both the results from Henderson, et al.(2003) and the results obtained in this study indicate), then we can analytically determine the conditions required for bifurcations by using the analytical approach presented in Section 2.1.2. The jet catches up to the Mach stem when $v_2$ - $v_3$ (the velocity of the jet towards the Mach stem with respect to point B) exceeds the velocity of the Mach stem with respect to point B. The velocity of the Mach stem with respect to B is equal to the velocity of B with respect to the Mach stem. The velocity of B with respect to the triple point is $v_3$; thus the velocity of B with respect to the Mach stem is equal to the component of $v_3$ normal to the Mach stem, labelled $v_{3n}$. So, the jet can reach the Mach stem when $v_2 - v_3 > v_{3n}$. We thus analytically determined the parameters for which $v_2 - v_3 = v_{3n}$ by using the MATLAB numerical computing environment (MATLAB 7.9.0 [Computer Software] 2009). The script is presented in Appendix B. By doing this analysis, we obtained analytical bifurcation transition points, which are presented in Figure 29.

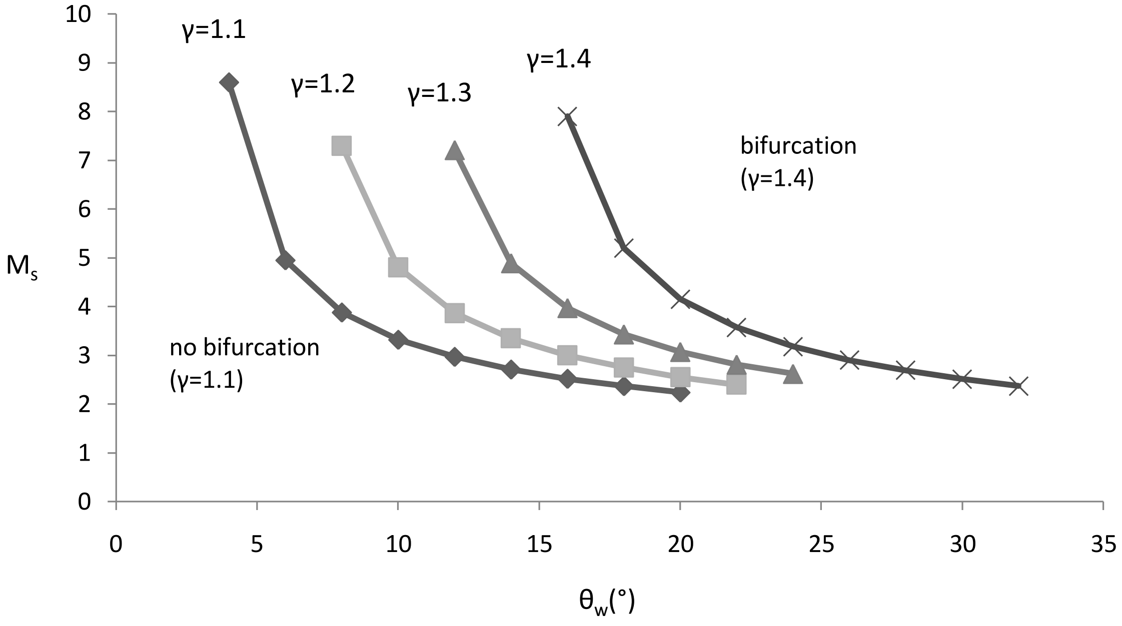

**Figure 29: Bifurcation transition points obtained by using the analytical method described above for *γ*=1.1, 1.2, 1.3, and 1.4. Lines connect the points to show the bifurcation boundary. Shock reflections with parameters below and to the left of a line are not predicted to have bifurcations, while shock reflections with parameters above and to the right of a line are predicted to have bifurcations.**

As would be expected, the analytical method predicts bifurcations earlier (i.e. for lower angles, all other parameters being equal) than the numerical solution does primarily because the analytical method does not take into account the vortex (see Figure 16 for instance) that forms in reality. However, both methods agree qualitatively. The analytical method clarifies the mechanism that causes bifurcations: when the slip line curves forward (due to a large enough pressure from the flow deflection process), and when the velocity difference across the slip line ($v_2$ - $v_3$) is sufficiently large such that it drives a wall jet which forms a vortex that affects the Mach stem, then a bifurcation is formed.

### 2.6.3 Bifurcation disappearance in the double Mach reflection regime

As is well known, a double Mach reflection has a second triple point. The “reflected” shock (labelled r’) of this second triple point intersects the slip line and thus affects the flow in region 2 (see Figure 14). At low ramp angles, this “reflected” shock r’ non-isentropically increases the pressure in region 2, and thus disturbs the pressure balance across the slip line s, and the slip line starts to bend at the r’-s intersection. However, as the ramp angle is increased, the reflected shock r' gets closer and closer to intersecting the wall (in order to match the solutions in the white and the grey regions) in addition to intersecting the slip line (see Figure 17). When this occurs, r' becomes an oblique shock for the flow in region 2, and the flow in region 2 can become parallel to the wall without the slip line curving towards the Mach stem. This provides an explanation for why bifurcations disappear before regular reflections occur.

### 2.6.4 Comparison of numerical results with physical experiments

While the model neglects diffusive phenomena, real shock reflection phenomena may be influenced by such effects. The effects of viscosity and conductivity would be felt across the slip line, as well as at the wall. This is because there is a velocity and temperature gradient at these surfaces, and viscosity and conductivity would have the effect of transferring momentum and energy across these surfaces. This would have the effect of smearing the velocity difference across the slip line ($v_2$ - $v_3$), as well as slowing down the wall jet thus reducing the size of the vortex, and consequently the onset of a bifurcation would be delayed.

The model also neglects real gas effects, but it is clear that real gas effects influence the shock reflection solution (see Ben-Dor (2007) for instance). However the effect that a real gas would have on the onset of bifurcations is unclear without doing a thorough analysis.

The fact that a higher Mach number (or a higher ramp angle, or a lower $\gamma$) is needed to obtain a bifurcation in reality is demonstrated well in the validation study shown in Section 2.3. In that section a numerically obtained Schlieren image was compared to an experimentally obtained interferogram from Glaz, et al.(1985). A vortex can be seen in both cases; however, there is a prominent bifurcation in the simulation case while there is only a slight bend to the Mach stem in the experimental case.

### 2.6.5 Effects of resolution and solver

It is of interest to discuss the effect that resolution had on the prominence of the Mach stem kink. Figure 21 showed that the kink was least prominent when *r* = 2 and *r* = 6, and most prominent for *r* = 3 - 5. The fact that the low resolution of *r* = 2 yielded a less prominent kink can be explained by “numerical viscosity”. “Numerical viscosity” is due to the finite resolution grid which cannot perfectly capture discontinuous phenomena, such as the slip line. Therefore, the slip line gets smeared, and becomes comparable to a mixing layer. As one would expect, “numerical viscosity” has a larger effect at lower resolutions, and thus the kink is less prominent at lower resolutions. It is important to note that numerical viscosity was not induced at the wall in the numerical simulations since the no-slip condition necessary for a boundary layer to form was not invoked. The fact that the kink at *r* = 6 is less prominent than at *r* = 3 - 5 is counterintuitive based on the above reasoning; there must be a new mechanism that operates at higher resolutions. Indeed, by observing Figure 21 it is clear that there are more vortices resolved along the slip line as the resolution is increased. These vortices are caused by the Kelvin-Helmholtz instability which is due to the velocity difference across the slip line. In other words, some of the flow’s kinetic energy is used to form vortices, and thus the velocity difference across the slip line is reduced. This explains why the kink is less prominent at higher resolutions.

# 3 Part 2: Bifurcations in detonations

## 3.1 Proposed model of triple point reflection as inert shock reflection

In order to investigate whether the bifurcations observed after triple point reflections in numerical simulations of detonations are a result of the inert shock reflection phenomenon, a model of the triple point reflection process as an inert shock reflection is proposed here.

The problem of symmetric triple points colliding has been previously modelled by Oppenheim et al. (1968) as one triple point reflecting off of a wall as shown in Figure 30. The wall corresponds to the axis of symmetry of the colliding triple points. Using $\varphi_1$ and $M_0$ obtained from experiments, the three shock theory presented in Section 2.1.2 can be applied to the three shock structure before the collision, and therefore the state of the gas in zones 1, 2, and 3 can be determined. Using the fact that the Mach stem just before collision (m) is equivalent to the incident shock just after collision (i') (thus $p_3=p_1$, and $\theta=\theta'$), the three shock theory can be again applied to determine the state of the gas in zones 1', 2', and 3'. The model neglects the effects of heat release and unsteadiness, therefore it only holds for short times after the reflection. For more details, see Oppenheim et al. (1968).

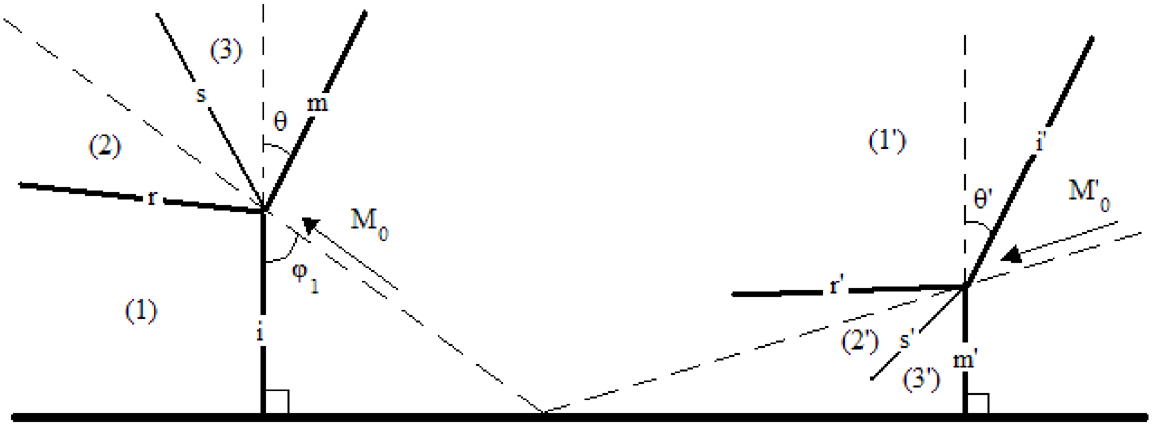

**Figure 30: Model for symmetric triple point collision used by Oppenheim et al. (1968).**

The post reflection triple point structure in Oppenheim's model is strictly a result of the new incident shock (or old Mach stem) reflecting off of the axis of symmetry. In other words, Oppenheim's model neglects the effects of the trailing transverse shock and slip line interactions on the detonation front, and thus the model can be further simplified to an incident shock reflecting off of a wall, as shown in Figure 31. This is the model that will be used in this study.

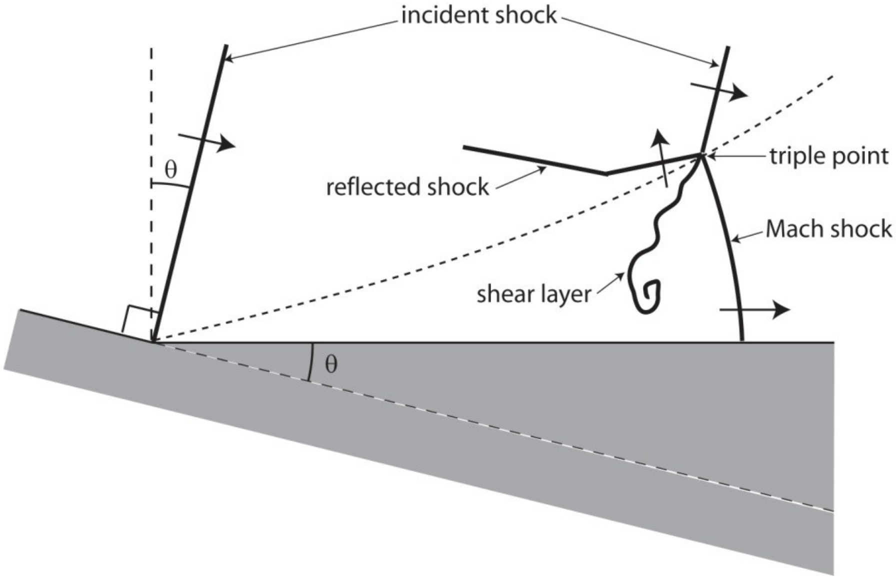

**Figure 31: Simplified version of Oppenheim's triple point reflection model used in this study.**

The model is equivalent to the problem studied in part 1 of this thesis; the Mach number of the incident shock at time of collision ($M_{sd}$) corresponds to the incident shock Mach number ($M_s$), the inclination angle of the incident shock at time of collision ($\theta$) corresponds to the ramp angle ($\theta_w$), and the specific heat ratio of the detonable mixture corresponds to $\gamma$.

It is known based on the results from part 1 that bifurcations can occur as a result of this model. However, it is unclear whether the model accurately captures the front of the reflected triple point since it neglects the effects of the trailing transverse shock and slip line interactions. Therefore, the model needs to be validated in order to investigate whether bifurcations in detonations originate from the inert shock reflection process.

## 3.2 Validation of proposed model

In order to obtain the input parameters necessary for the proposed triple point reflection model ($M_{sd}$ and $\theta$), a cellular detonation simulation was conducted first. The numerical details and results are presented in Sections 3.2.1 and 3.2.2 respectively. The numerical details of the triple point reflection model simulation are presented in Section 3.2.3. The comparison of the results from the model simulation with the results from the detonation simulation is presented in Section 3.2.4. This comparison clarifies whether the model captures the detonation front after the triple point reflection accurately. In order to confirm that the model accurately predicts bifurcations in detonations, numerical simulations of other detonable mixtures and their triple point reflection models were conducted, and the results are shown in Section 3.2.5.

### 3.2.1 Cellular detonation simulation details

The entire detonation flow field is assumed to be well captured by the Euler equations for a perfect reacting gas with constant specific heats and molecular weight:

$$\frac{D\rho}{Dt} + \rho\nabla \cdot U = 0;\;\; \rho\frac{DU}{Dt} + \nabla p = 0;\;\; \rho\frac{De}{Dt} = \frac{p}{\rho}\frac{D\rho}{Dt} + \rho Q\frac{D\alpha}{Dt}$$

where $D/Dt$ denotes the material derivative $D/Dt \equiv \partial/\partial t + U \cdot \nabla$, $U$ is the velocity vector, $Q$ is the total energy release per unit mass and $\alpha$ is the progress variable of the chemical energy release, which takes a value of 1 in the reactants and 0 in the products. The internal energy is given by $e=RT/(\gamma-1)$, where the temperature can be found from the ideal gas law, $p=\rho RT$.

For simplicity, the rate of energy release is modeled by a first order one-step reaction with Arrhenius dependence on temperature:

$$\frac{D\alpha}{Dt} = k(\alpha - 1)e^{-\frac{E_a}{RT}}$$

where $k$ is the pre-exponential factor, and $E_a$ is the activation energy, which characterizes the reaction rate's sensitivity to temperature perturbations The pre-exponential factor $k$ was set such that the half reaction length $\Delta_{1/2}$, (the distance from the shock to the point where half of the heat is released in the steady one-dimensional, or ZND detonation wave-see Lee (2008) for more details on the ZND detonation wave) corresponds to unity distance. Hence all distances are normalized by $\Delta_{1/2}$. Nondimensionalization of the governing equations uses the initial pressure $p_0$ as pressure scale, $\rho_0$ as density scale, and correspondingly $(p_0/\rho_0)^{1/2}$ as velocity scale. For reference, the resulting time scale is thus $\Delta_{1/2}/(p_0/\rho_0)^{1/2}$.The free parameters of our model were chosen as $E_a/RT_0$ =27and $Q/RT_0$ =50 and $\gamma$=1.2. These are parameters representative of an irregular detonation which have yielded bifurcations in the past (Radulescu, Sharpe, et al. 2007).

The detonation simulations were conducted on a domain that is 1000 $\Delta_{1/2}$ long and 20 $\Delta_{1/2}$ in width. As initial condition, the ZND detonation structure was placed at a distance of 30 $\Delta_{1/2}$ away from the rear boundary. Random initial perturbations in the reaction progress variable $\alpha$ with no preferred length scale, placed at 40 $\Delta_{1/2}$ from the rear boundary, were used to generate the incipient source of instability (Sharpe and Quirk 2008). The top and bottom boundary conditions used reflective conditions.

The model detailed above was solved using the AMRITA software development system, developed by Quirk (1998). Roe's scheme was used as the solver. An adaptive mesh-refinement technique was used to obtain sufficient grid resolution to capture the reaction zone. The base grid spacing corresponded to 1 $\Delta_{1/2}$. The finest grid consisted of 64 grid points per $\Delta_{1/2}$, which covered the entire reaction zone. The temporal resolution was controlled by the CFL number, which was set to 0.5. The same script has been used for calculating detonation dynamics in the past (Sharpe and Quirk 2008), and is shown in Appendix C.

### 3.2.2 Cellular detonation simulation results

The results of the cellular detonation simulation ($E_a/RT_0$=27, $Q/RT_0$=50, $\gamma$ =1.2) are presented here. Figure 32 is an integrated vorticity plot (a numerical method to obtain a soot foil) which illustrates the irregular cellular structure of this detonation.

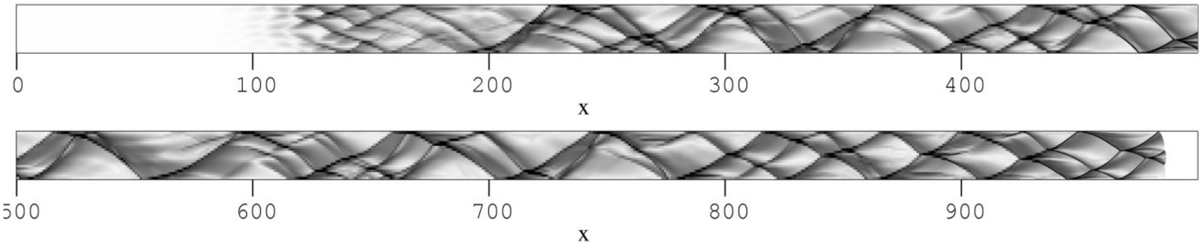

**Figure 32: Integrated vorticity plot (i.e. numerical soot foil) obtained from the detonation simulation with $E_a/RT_0$=27, $Q/RT_0$=50, $\gamma$=1.2. The domain is 1000 $\Delta_{1/2}$ long by 20 $\Delta_{1/2}$ wide.**

Figure 33 shows density plots at three different times, focusing on the triple point reflection off of the bottom wall at $x$=907.77, similar to the one shown in the introduction. The plots correspond to when the Mach stem is 1.86 $\Delta_{1/2}$ past the reflection, 4.28 $\Delta_{1/2}$ past the reflection, and 8.68 $\Delta_{1/2}$ past the reflection. There does not seem to be a bifurcation in Figure 33-1 (at this point the Mach shock is not adequately resolved); however, Figure 33-2 and Figure 33-3 show bifurcations to the Mach shock. In fact, the bifurcation in Figure 33-3 appears more prominent than the one in Figure 33-2.

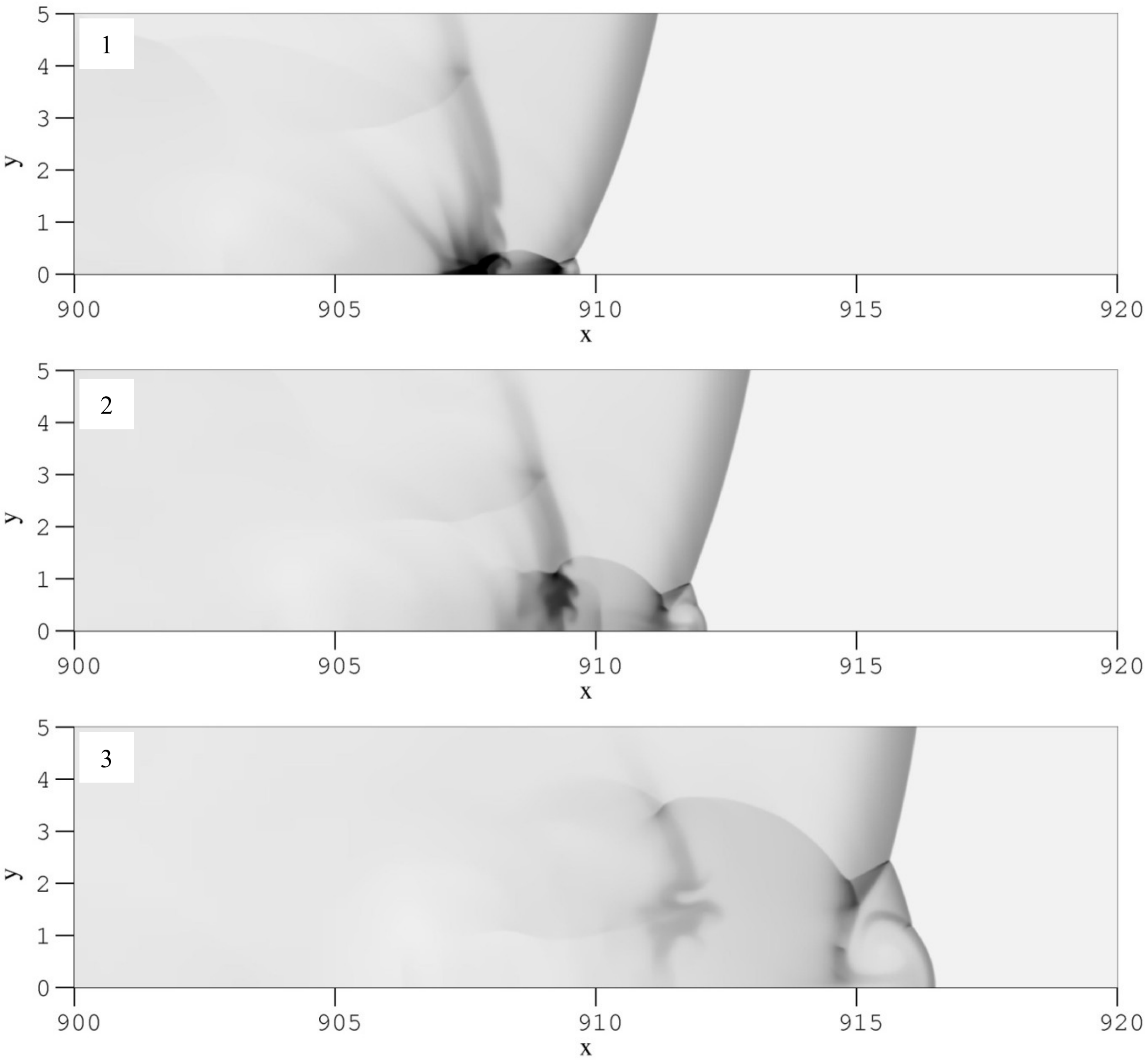

**Figure 33: Density plots at three times after a triple point reflection off of the bottom wall at $x$=907.77. The Mach stem is 1.86 $\Delta_{1/2}$ past the reflection, 4.28 $\Delta_{1/2}$ past the reflection, and 8.68 $\Delta_{1/2}$ past the reflection in plots 1), 2) and 3) respectively.**

Figure 34 shows what happens to the bifurcation at even later times. Namely, the density plots when the Mach stem is 13 $\Delta_{1/2}$ past the reflection, 20.94 $\Delta_{1/2}$ past the reflection, and 27.38 $\Delta_{1/2}$ past the reflection are shown in Figure 34-1, Figure 34-2, and Figure 34-3 respectively. The bifurcation is still quite prominent in Figure 34-1, is weaker in Figure 34-2, and has essentially disappeared in Figure 34-3.

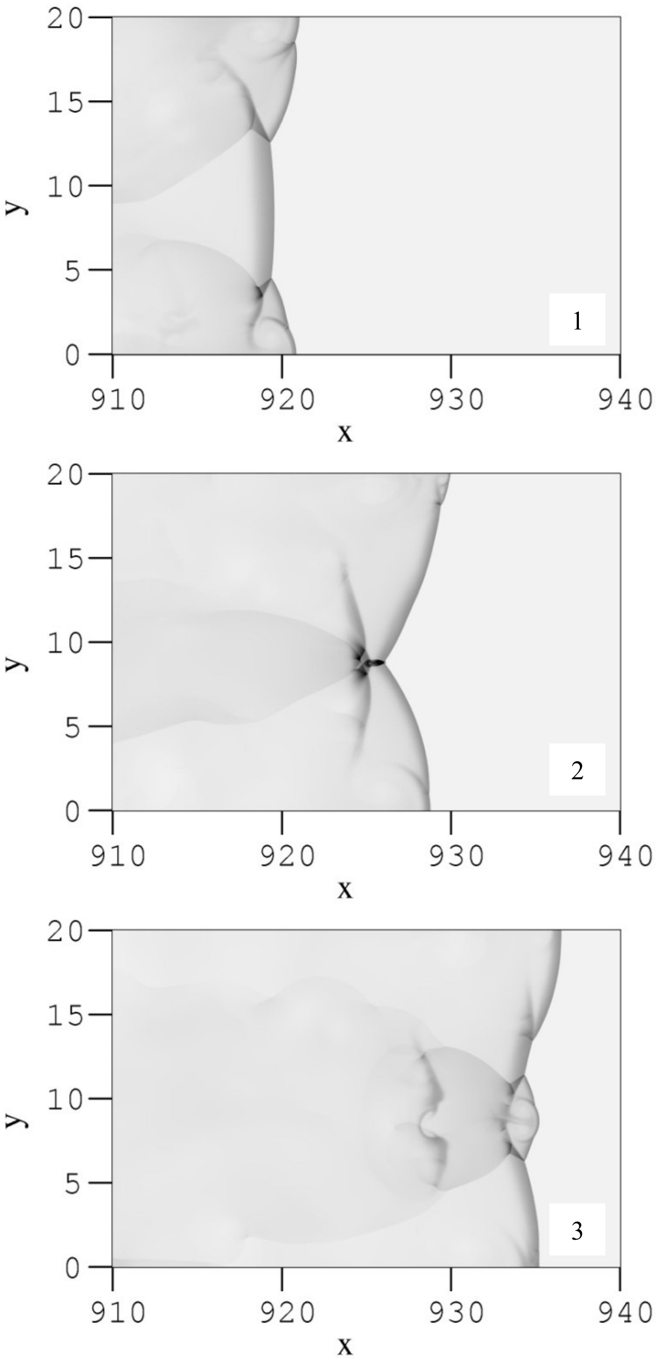

**Figure 34: Density plots at three times after a triple point reflection off of the bottom wall. The Mach stem is 13 $\Delta_{1/2}$ past the reflection, 20.94 $\Delta_{1/2}$ past the reflection, and 27.38 $\Delta_{1/2}$ past the reflection in plots 1), 2) and 3) respectively.**

### 3.2.3 Triple point reflection model simulation details

We now proceed with the comparison of the flowfields obtained above with the ones obtained by the triple point reflection model of Figure 31.

The numerical details for the triple point reflection model simulation were essentially the same as the ones used for the inert shock reflection simulations in part 1 of this study. These details can be found in Section 2.2. The primary difference was that the finest grid consisted of 64 grid points per base grid, and the CFL number was set to 0.5 in order to match the resolution of the cellular detonation simulations. The domain was also adapted for better comparison: the domain that had 24 base grid points in the *x* direction by 7 base grid points in the *y* direction, the base of the ramp was positioned at the 16th base grid point in the *x* direction, and the shock wave was initially placed at the 8th base grid point in the *x* direction. The full AMRITA script can be found in Appendix D.

From the cellular detonation simulation results, it was found that $M_{sd}$=6.43 and $\theta$=34°. Therefore, the input parameters for the model were $M_s$=6.43, $\theta_w$=34°, and $\gamma$=1.2.

### 3.2.4 Comparison of results with detonation simulation

The results of the triple point reflection model simulation were compared to the results of the cellular detonation simulation to see if the model is indeed valid. The density plots of the triple point reflection model simulation when the Mach stem is approximately 2 grid points past the reflection, 4.3 grid points past the reflection, and 8.5 grid points past the reflection are shown in Figure 35-1a, Figure 35-2a, and Figure 35-3a respectively. The corresponding cellular detonation density plots (where 1 base grid point is equivalent to 1 $\Delta_{1/2}$) are shown in Figure 35-1b, Figure 35-2b, and Figure 35-3b at the same scale as their counterparts. Figure 35-1a and Figure 35-1b look roughly the same; the size of the Mach shocks and the density profiles are relatively similar. This indicates that our model for triple point reflection works well up to this point. At this early time, a bifurcation is not observed in either case due to the low resolution. Figure 35-2a and Figure 35-2b both have a similar bifurcation, but the size of the Mach shocks and the density profiles are more dissimilar. Figure 35-3a and Figure 35-3b look even less similar, but a bifurcation is still observed in both cases. For a more complete quantitative comparison, a graph of the pressure behind the Mach shock versus the Mach shock distance from the reflection point is shown in Figure 36 for both the triple point reflection model and the cellular detonation simulations. It is clear from this graph that at early times the triple point reflection model works well, and at later times (approximately when the Mach shock is 2 $\Delta_{1/2}$ past the reflection) the triple point reflection model and the cellular detonation simulations diverge. It can be concluded that the triple point reflection model is valid at early times, before heat release and a substantial decay of the Mach shock occurs in the detonation simulation.

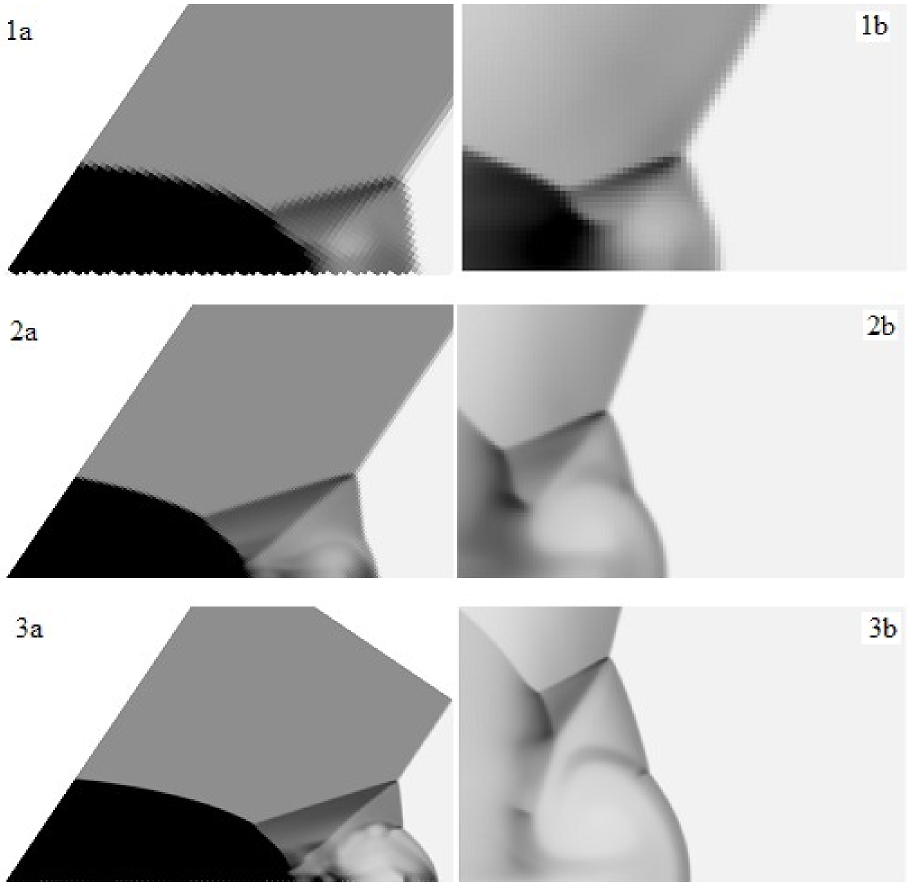

**Figure 35: Density plots obtained from the triple point reflection model (labelled a) and the cellular detonation (labelled b) simulations at three times after reflection. The Mach stem is approximately 2 grid points (or $\Delta_{1/2}$ ) past the reflection in (1a) and (1b), approximately 4.3 grid points past the reflection in (2a) and (2b), and approximately 8.5 grid points past the reflection in (3a) and (3b). Corresponding plots are at the same scale.**

**Figure 36: Pressure behind the Mach shock, $p_3$, versus the Mach shock distance from the reflection point for both the triple point reflection model simulation and the cellular detonation simulation.**

### 3.2.5 Prediction of bifurcations in various detonable mixtures

Based on the results of the previous section, it is clear that the model is valid at early times, but it is not clear whether the model predicts bifurcations, or the absence of bifurcations, accurately. In order to verify that the model works to predict bifurcations, the model was tested against two other detonable mixtures (mixture 1: $E_a/RT_0$=47.42, $Q/RT_0$=26.74, $\gamma$=1.4; mixture 2: $E_a/RT_0$=72.55, $Q/RT_0$=17.2, $\gamma$=1.66). The parameters $E_a/RT_0$ and $Q/RT_0$ were set so that $E_a/RT_{VN}$, where $VN$ is the von Neumann state of a ZND detonation, and $M_{CJ}$, the CJ Mach number, were the same in all three cases (see Lee (2008) for details on ZND detonations and the CJ Mach number). The variation in $\gamma$ was done since it is known from part 1 that bifurcation appearance is highly dependent on $\gamma$. For the model, it was assumed that the angle of incidence of the incident shock at the time of reflection, $\theta$, was 34° degrees, and the Mach number of the incident shock at the time of reflection, $M_{sd}$, was the CJ Mach number, 6.22. These assumptions were made based on studying a few of the triple point reflections of the detonation simulation results of the $\gamma$=1.2 case. Therefore, the input parameters for the model were $M_s$=6.22, $\theta_w$=34°, and $\gamma$=1.4 for mixture 1, and $M_s$=6.22, $\theta_w$=34°, and $\gamma$=1.4 for mixture 2.

The detonation and model simulations were run with the same details as discussed in Sections 3.2.1 and 3.2.3. The input parameters were simply changed to the ones discussed above. A triple point reflection off a wall was isolated near the end of the detonation simulation in both cases. The density plots from the model and detonation simulations of the $\gamma$=1.4, and $\gamma$=1.66 case when the Mach stem is roughly 8 grid points (or $\Delta_{1/2}$) past the reflection point are shown in Figure 37. It can be seen that bifurcations are not observed in the model simulation, or in the detonation simulation in both cases. It had already been found in the previous section that a bifurcation was observed by the model and the detonation simulation in the $\gamma$=1.2 case. It can be concluded that the model predicts bifurcations relatively accurately.

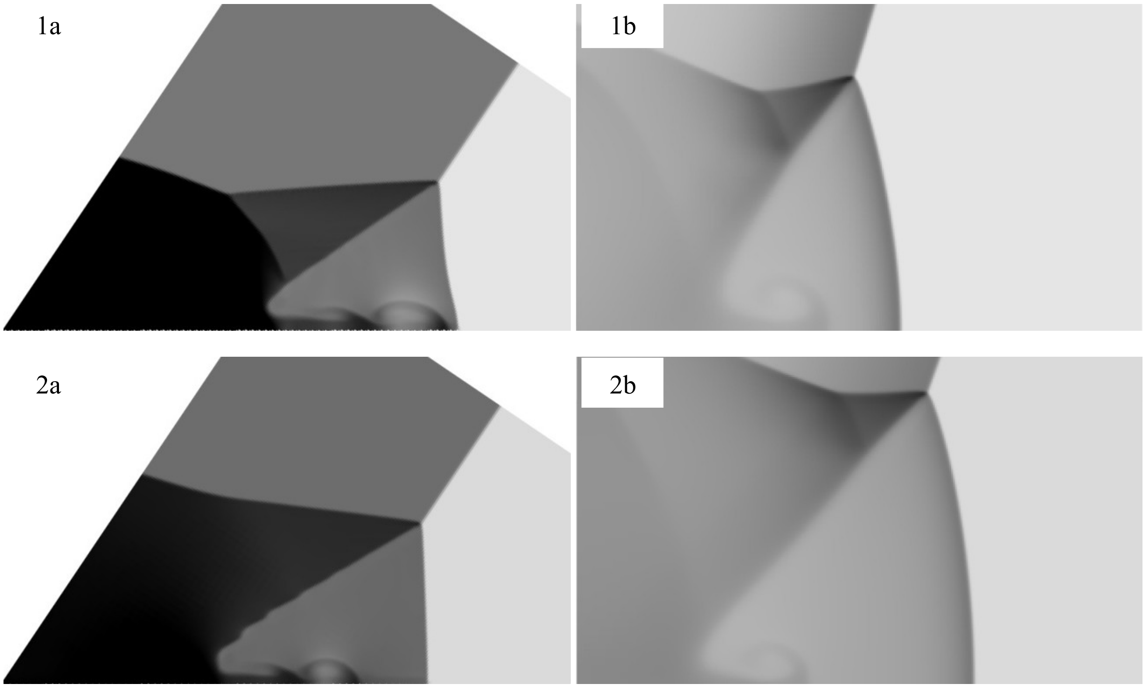

**Figure 37: Density plots obtained from the triple point reflection model (labelled a) and the cellular detonation (labelled b) simulations. (1a) and (1b) correspond to the $\gamma$=1.4 case, and (2a) and (2b) correspond to the $\gamma$=1.66 case. The images were taken when the Mach stem was roughly 8 grid points (or $\Delta_{1/2}$) past the reflection point. All Plots are at the same scale.**

## 3.3 Discussion: Effect of bifurcations on irregularity

As was mentioned in the introduction, it is likely that bifurcations contribute to irregularity because they seem to only occur in irregular detonations, and they are a source of new triple points. It is of interest to determine whether they do since irregular mixtures behave differently than regular mixtures. Namely, irregular mixtures have a more turbulent reaction zone (Shepherd 2009), and are more difficult to quench (Radulescu and Lee 2002).

It is clear that bifurcations are a source of new triple points, or transverse waves. However, if these new triple points disappear before they interact with other triple points, then they would not directly affect irregularity since no new cells would form. A closer inspection of the results from the detonation simulation shown in Section 3.2.2 reveals that a new cell can form directly as a result of bifurcations. The sequence which leads to a new cell forming is shown in Figure 38 and has been studied in detail in (Mach and Radulescu 2011). At the start of this section, two triple points, which had just collided with each other, can be seen, labelled (1) and (2). Two bifurcations can also be seen, labelled (3) and (4). Triple point (1) reflects off of the top wall and becomes triple point (5) with a bifurcation, labelled (6). Bifurcation (4) survives to interact with triple point (5). The interaction gives rise to a stronger upward propagating triple point labelled (7). Bifurcation (6) and triple point (7) combine to form an even stronger triple point which reflects off of the top wall and continues on, thus forming a new cell.

The mechanism of new cell formation directly as a result of bifurcations discussed above is likely to be hampered by viscosity, and thus less likely to occur in experimental detonations. However, it is very possible that the bifurcation phenomenon indirectly leads to new cell formation; The perturbation of the reaction zone behind the Mach stem by the vortex itself, or by the likely turbulence in the vortex (demonstrated well by the high resolution simulations conducted by Mahmoudi and Mazaheri (2011)) could be amplified by the inherent instability of detonations driven by the reaction rate’s sensitivity to temperature perturbations, and thus indirectly lead to irregularity.

**Figure 38: An integrated vorticity plot (i.e. soot foil) of the section 890<x<945 is shown in (1), and density plots of when the front is at 4 consecutive positions in this section are shown in (2), (3), (4) and (5). Together they show how a bifurcation survives to become a new triple point.**

### 3.3.1 Comparison of bifurcation prediction with experimental evidence of irregularity

In order to determine whether bifurcations effect experimental irregularity, bifurcation prediction was compared to experimental evidence of irregularity. The bifurcation prediction was done by applying the triple point reflection model to numerous detonable mixtures. In order to apply the model, representative values of $M_{sd}$, $\gamma$, and $\theta$ for the various detonable mixtures had to be obtained. The CJ Mach number, $M_{CJ}$, was assumed to be equivalent to $M_{sd}$ since results of the cellular detonation simulation shown in Section 3.2.2 revealed that the incident shock strength at the moment of collision is close to the $M_{CJ}$. Since $\gamma$ in reality is a function of temperature and thus takes on different values before and after a shock, an assumption for $\gamma$ had to be made. The post incident shock $\gamma$ was selected in order to accurately capture the compressibility in the shocked gases where the wave phenomenon leading to bifurcations occurs. $\theta$ was assumed to be of 34° for all detonations since this is what was found in the cellular detonation simulation results shown in Section 3.2.2. The CJ Mach number for the mixture was calculated with NASA's CEA program (Gordon and McBride 1994). The CEA program was then used to calculate the post shock $\gamma$ for the mixture travelling at the CJ Mach number, $M_{CJ}$. Once $M_{sd}$, $\gamma$, and $\theta$ were determined, the results from part 1, namely Figure 19, were then used to predict bifurcation occurrence.

The results are presented in Table 1. The prediction of bifurcation was most sensitive to $\gamma$, since $\theta_w$ was the same for all predictions, and $M_s$ only varied from 4.24-6.93. Basically, $\gamma$ below 1.4 meant bifurcations were predicted, and above 1.4 meant bifurcations were not predicted. It is clear that bifurcations are predicted to only occur in irregular detonations.

**Table 1: Experimental evidence of regularity and bifurcation prediction. Source 1 is Austin (2003), 2 is Manzhalei (1977), 3 is Moen, Funk, et al. (1984), and 4 is Moen, Murray, et al. (1982). MCJ and $\gamma$ were calculated using NASA's CEA program (Gordon and McBride 1994). Bifurcation prediction was made by applying the model (by making assumptions for $M_{sd}$, $\gamma$, and $\theta$), and then using the results from part 1.**

| Mixture | $P_0$ (bar) | Soot foil | Source | $M_{CJ}$ | $\gamma$ (post shock) | Bifurcation predicted |
|---|---|---|---|---|---|---|
| $2H_2$-$O_2$-12Ar | 0.2 | Regular | 1 | 4.48 | 1.54 | No |
| $2H_2$-$O_2$-17Ar | 0.2 | Regular | 1 | 4.24 | 1.57 | No |
| $2H_2$-$O_2$-$3.5N_2$ | 0.2 | Irregular | 1 | 4.77 | 1.32 | Yes |
| $2H_2$-$O_2$-$5.6N_2$ | 0.2 | Irregular | 1 | 4.57 | 1.32 | Yes |
| $H_2$-$N_2O$-$1.33N_2$ | 0.2 | Irregular | 1 | 5.51 | 1.25 | Yes |
| $H_2$-$N_2O$-$1.77N_2$ | 0.2 | Irregular | 1 | 5.36 | 1.26 | Yes |
| $C_2H_4$-$3O_2$-$8N_2$ | 0.2 | Irregular | 1 | 5.45 | 1.25 | Yes |
| $C_2H_4$-$3O_2$-$10.5N_2$ | 0.2 | Irregular | 1 | 5.25 | 1.26 | Yes |
| $C_3H_8$-$5O_2$-$9N_2$ | 0.2 | Irregular | 1 | 5.83 | 1.21 | Yes |
| $2H_2$-$O_2$ | 0.1 | Intermediate | 2 | 5.04 | 1.32 | Yes |
| $2H_2$-$O_2$-3Ar | 0.075 | Regular | 2 | 4.83 | 1.42 | No |
| $2H_2$-$O_2$-7Ar | 1 | Regular | 2 | 4.84 | 1.49 | No |
| $H_2$-$3O_2$ | 1 | Irregular | 2 | 4.62 | 1.31 | Yes |
| $C_2H_2$-$2.5O_2$ | 0.075 | Intermediate | 2 | 6.93 | 1.20 | Yes |
| $C_2H_2$-$2.5O_2$-10.5Ar | 1 | Regular | 2 | 5.59 | 1.41 | No |
| $C_2H_2$-$24O_2$ | 0.1 | Irregular | 2 | 4.52 | 1.29 | Yes |
| $4NH_3$-$3O_2$ | 1 | Irregular | 2 | 6.53 | 1.17 | Yes |
| $C_2H_2$-$15O_2$ | 1 | Irregular | 2 | 5.16 | 1.27 | Yes |
| $C_2H_2$-air (stoich.) | 1 | Irregular | 2 | 5.41 | 1.27 | Yes |
| $CH_4$-$2O_2$ | 1 | Irregular | 2 | 6.73 | 1.17 | Yes |
| $CH_4$-$2O_2$-2Ar | 0.1 | Irregular | 2 | 5.79 | 1.24 | Yes |
| $CH_4$-air (stoich.) | 1 | Irregular | 3 | 5.11 | 1.26 | Yes |
| $C_3H_8$-air (stoich.) | 1 | Irregular | 3 | 5.31 | 1.24 | Yes |
| $C_2H_4$-air (stoich.) | 1 | Irregular | 4 | 5.29 | 1.26 | Yes |

Due to the effect of viscosity, it is likely that the correlation found between bifurcation prediction and irregularity is not perfect. Nevertheless, the vortex will be closer to Mach stem in irregular mixtures than in regular mixtures, and thus the reaction zone will be more perturbed by the vortex in irregular mixtures. Irregular mixtures have already been correlated with a high reaction rate sensitivity to temperature perturbations. It is thus interesting that the perturbations to the reaction zone driven by the bifurcation phenomenon, and the high instability driven by the sensitivity of the reaction rate to perturbations occur in the same (irregular) mixtures. This could potentially or partially explain the substantial difference between regular and irregular detonations.

# 4 Conclusions

This thesis has focused on bifurcations of the Mach shock in unsteady shock reflections. Namely, part 1 of this thesis was focused on bifurcations that occur as a result of shock reflections, and part 2 of this thesis was focused on the bifurcations that occur as a result of triple point reflections in detonations.

In part 1, it was numerically found that for inert shock reflections, bifurcations of the Mach shock occur when the incident Mach number is high, the ramp angle is high, and $\gamma$ is low. It was clarified in the discussion that bifurcations occur when the slip line curves forward (due to a large enough pressure from the flow deflection process), and when the velocity difference across the slip line ($v_2 - v_3$) is sufficiently large such that it drives a wall jet which forms a vortex that affects the Mach stem. It is expected that the numerically obtained bifurcation transition boundaries obtained for an inviscid, non-heat conducting perfect gas are qualitatively correct, but not quantitatively correct. More work is required to address this open issue.

In part 2, a detonation triple point reflection was modelled as an inert shock reflecting off of a wall. It was found that the model accurately captures the front of the detonation at early times after the reflection, and accurately predicts bifurcations. It can thus be concluded that the inert shock reflection process is the cause of bifurcations in detonations. A closer inspection of the results of the cellular detonation simulation revealed that bifurcations can directly lead to new cells forming. Another investigation revealed that bifurcations are predicted to only occur in irregular mixtures. It is thus likely that bifurcations contribute irregularity, but the extent of their effect is unclear, and should be subject to further investigation.

# References

Austin, JM. "The role of instability in gaseous detonation." PhD Thesis, California Institute of Technology, 2003.

Ben-Dor, G. *Shock wave reflection phenomena.* New York: Springer, 2007.

Colella, P, and HM Glaz. "Numerical calculation of complex shock reflections in gases." *Lecture Notes in Physics* 218 (1985): 154-158.

Deiterding, R. "Parallel adaptive simulation of multi-dimensional detonation structures." PhD thesis, Brandenburgischen Technischen Universitat Cottbus., 2003.

Einfeldt, B. "On Godunov-type methods for gas-dynamics." *SIAM Journal of Numerical Analysis* 25, no. 2 (1988): 294-318.

Glaz, HM, P Colella, II Glass, and RL Deschambault. "A numerical study of oblique shock-wave reflections with experimental comparisons." *Proceedings of the Royal Society of London. Series A* 398 (1985): 117-140.

Godunov, SK. "A difference scheme for numerical solution of discontinuous solution of hydrodynamic equations." *Math. Sbornik* 47 (1959): 271-306.

Gordon, S, and BJ McBride. "Computer program for calculation of complex chemical equilibrium compositions and applications." NASA Reference Publication 1311, 1994.

Henderson, LF, EI Vasilev, G Ben-Dor, and T Elperin. "The wall-jetting effect in Mach reflection: theoretical consideration and numerical investigation." *Journal of Fluid Mechanics* 479 (2003): 259-286.

Hornung, H. "Regular and Mach reflection of shock waves." *Annual Review of Fluid Mechanics* 18 (1986): 33-58.

Hu, XY, BC Khoo, DL Zhang, and ZL Jiang. "The cellular structure of a two-dimensional H2/O2/Ar detonation wave." *Combustion theory and modelling* 8, no. 2 (2004): 339-359.

Law, CK, and II Glass. "Diffraction of strong shock waves by a sharp compressive corner." *CASI Transactions* 4, no. 1 (1971): 2-12.

Lee, JHS. *The detonation phenomenon.* New York: Cambridge Unversity Press, 2008.

Liang, Z, S Browne, R Deiterding, and JE Shepherd. "Detonation front structure and the competition for radicals." *Proceedings of the Combustion Institute* 31 (2007): 2445-2453.

Liou, MS, and CJ Steffen. "A new flux splitting scheme." *Journal of Computational Physics* 107, no. 1 (1993): 23-39.

Mach, P, and MI Radulescu. "Mach reflection bifurcations as a mechanism of cell multiplication in gaseous detonations." *33rd International Combustion Symposium.* 2011. 2279-2285.

Mahmoudi, Y, and K Mazaheri. "High resolution numerical simulation of the structure of 2-D gaseous detonations." *Proceedings of the Combustion Institute.* 2011. 2187-2194.

Manzhalei, VI. "Fine structure of the leading front of a gas detonation." *Fizika Goreniya i Vzryva* 13, no. 3 (1977): 470-472.

*MATLAB 7.9.0 [Computer Software].* MathWorks. Natick, MA, USA, 2009.

Moen, IO, JW Funk, SA Ward, and GM Rude. "Detonation length scales of fuel-air explosives." *Progress in Astronautics and Aeronautics* 94 (1984): 55-79.

Moen, IO, SB Murray, D Bjerketvedt, A Rinnan, R Knystautas, and JHS Lee. "Diffraction of detonation from tubes into a large fuel-air explosive cloud." *19th Symposium (International) on Combustion Proceedings*, 1982: 635-644.

Oppenheim, AK, JJ Smolen, and LJ Zajac. "Vector polar method for the analysis of wave intersections." *Combustion and Flame* 12, no. 1 (1968): 63-76.

Pullin, DI. "Direct numerical simulation methods for compressible inviscid ideal-gas flow." *Journal of Computation Physics* 34, no. 2 (1980): 231-244.

Quirk, JJ. "AMRITA: A computational facility (for CFD modelling)." *29th Computational Fluid Dynamics, von Karman Institute Lecture Series* 3 (1998): D1-D72.

Radulescu, MI. "The propagation and failure mechanism of gaseous detonations: experiments in porous-walled tubes." PhD Thesis, Department of Mechanical Engineering, McGill University, 2003.

Radulescu, MI, and JHS Lee. "The failure mechanism of gaseous detonations: experiments in porous wall tubes." *Combustion and Flame* 131 (2002): 29-46.

Radulescu, MI, GJ Sharpe, CK Law, and JHS Lee. "The hydrodynamic structure of unstable cellular detonations." *Journal of Fluid Mechanics* 580 (2007): 31-81.

Roe, PL. "Approximate riemann solvers, parameter vectors and difference schemes." *Journal of Computational Physics* 43, no. 2 (1981): 357-372.

Semenov, AN, MK Berezkina, and IV Krasofskaya. "Classification of shock wave reflections from a wedge. Part 2: Experimental and numerical simulations of different types of Mach reflections." *Technical Physics* 54, no. 4 (2009): 497-503.

Semenov, AN, MP Syshchikova, and MK Berezkina. *Zhurnal Tekhnicheskoi Fizik* 40, no. 5 (1970).

Sharpe, GJ. "Transverse waves in numerical simulations of cellular detonations." *Journal of Fluid Mechanics* 447 (2001): 31-51.

Sharpe, GJ, and JJ Quirk. "Nonlinear cellular dynamics of the idealized detonation model: Regular cells ." *Combustion Theory and Modelling* 12, no. 1 (2008): 1-21.

Shepherd, JE. "Detonations in gases." *Proceedings of the Combustion Institute* 32 (2009): 83-98.

Smith, LG. "Photographic investigation of the reflection of plane shocks in air." OSRD Report No. 6271, 1945.

Thompson, PA. *Compressible-Fluid Dynamics.* New York: McGraw-Hill, 1972.

White, D. "Turbulent structure of gaseous detonations." *Physics of fluids* 4 (1961): 465-480.

Xu, SJ, T Aslam, and DS Stewart. "High resolution numerical simulation of ideal and non-ideal compressible reacting flows with embedded internal boundaries." *Combustion Theory and Modelling* 1, no. 1 (1997): 113-142.

## Appendix A: AMRITA script for shock reflection simulations conducted in part 1

The script used by the AMRITA environment to simulate shock reflections is shown here. The title at the start of each fold indicates what each fold is accomplishing. In this study, all the parameters were kept constant except for $M_s$ (called “Ms” in the script), $\theta_w$ (called “angle” in the program), γ (called “gamma” in the script), and *r* (called “r” in the program). These parameters were manipulated in lines 158 to 161. Do loops were used to run multiple simulations consecutively. The solver was also varied in this study (between roe, godunov, efm, hlle, and ausm), and this was accomplished at line 150.

```
1    fold::amrita { define array sizes
2         ArraySizes {
3              #NGIxJ=25000000
4              #NEX=4000000
5              #NGD=100000
6              #NGIJ=10000000
7
8              #NL     = 100        # maximum number of grid levels
9              #NGD    = 280000      # maximum number of mesh patches
10             #NGIJ   = 7000000     # maximum number of perimeter cells
11             #NGIxJ  = 2000000    # maximum number of grid cells
12             #NEX    = 200000     # length of external boundaries table
13             #NBDYS  = 800000      # maximum number of scrunched boundaries
14             #NGHOST = 20         # number of ghost cells
15
16             NGIxJ = 2000000
17             NGD   = 8000
18
19        }
20   }
21   fold::amrita { run simulation
22     fold::amrita { prelims
23       EulerEquations {
24         space = 2D
25       }
26       fold::amrita { init resources
27         fold::amrita { get code
28           if(!&amrso("code")) then
29             fold::amrita { build code
30               BasicCodeGenerator {
31                 solver    = roe_fl
32                 scheme    = flux-limited'operator-split
33               }
34               foreach flux (godunov, efm, hlle, ausm)
35                 BasicCodeGenerator {
36                   solver    = $flux`_km
37                   flux      = bcg/$flux
```

```
          scheme    = kappa-muscl'operator-split
        }
      end foreach
    }
  endif
}
fold::amrita { DrawObstacleBody
  proc DrawObstacleBody {
    }
    plot amr_sol:axs::PSI[] contours L0.0 m<0>
    red   ::= amr_sol:axs::PSI[]<0 ? -1 : 69
    green ::= amr_sol:axs::PSI[]<0 ? -1 : 110
    blue  ::= amr_sol:axs::PSI[]<0 ? -1 : 150
    plot image {g0} RGB<red[],green[],blue[]>
  end proc
}
fold::amrita{ DensityGradientPlot
  proc DensityGradientPlot {
      exposure [0:1]     = 1.0  # darkness of image
      grid               = {G}  # select grid
      max                = 10.
      min               = 0.
      }
      DrhoDx      ::= (RHO[+i]-RHO[-i])/(X[+i]-X[-i])
      DrhoDy      ::= (RHO[+j]-RHO[-j])/(Y[+j]-Y[-j])
      schlieren   ::= sqrt(DrhoDx[]**2+DrhoDy[]**2)
      wt          ::= 1-((schlieren[]-$min)/($max-$min))
      wt          ::= wt[]>0 ? wt[] : 0
      greyshading ::= $exposure*wt[]
      plot image $grid m<greyshading[]>
  end proc
}
fold::amrita{ DensityPlot
  proc DensityPlot {
      exposure [0:1]     = 1.0  # darkness of image
      grid               = {G}  # select grid
      max                = 5.0
      min               = 1
      }
      wt          ::= 1-((RHO[]-$min)/($max-$min))
      wt          ::= wt[]>0 ? wt[] : 0
      greyshading ::= $exposure*wt[]
      plot image $grid m<greyshading[]>
  end proc
}
fold::amrita{ PressurePlot
  proc PressurePlot {
      exposure [0:1]     = 1.0  # darkness of image
      grid               = {G}  # select grid
      max                = 75
      min               = 1
      }
      wt          ::= 1-((P[]-$min)/($max-$min))
      wt          ::= wt[]>0 ? wt[] : 0
      greyshading ::= $exposure*wt[]
      plot image $grid m<greyshading[]>
```

```
      end proc
    }
    fold::amrita { InertShockReflectionProblem
      proc InertShockReflectionProblem {
          fold::amrita { parameters
            Ms       =  6.2     # shock strength
            gamma    =  1.2
            im       =  128      # base grid points in x-direction
            jm       =  64       # base grid points in y-direction
            Xs       =  16      # shock position
            lmax     =  2       # grid levels
            r        =  4     # refinement ratio
            X1       =  32      # location of the start of the ramp
            THETA    #= rad(20) # angle of the wedge
          }
        }
        fold::amr_sol'Domain{
          lscale    1
          patch <+,1,w$im,h$jm>
        }
        fold::amrita { Problem specific quantities
          specify GAMMA ::= $gamma
        }
        fold::amrita { Boundary Conditions
          W'quiescent  ::= <RHO=1,U=0,V=0,P=1>
          fold::amrita { get post-shock state
            ShockWave Ms=$Ms, state1=quiescent, state2=post_shock
          }
          fold::amr_sol'BoundaryConditions{
            Nbdy  domain: reflect
            Ebdy  domain: extrapolate
            Wbdy  domain: prescribe   W'post_shock
            Sbdy  domain: reflect
            AXS::InternalBoundary {
               PSI = ((tan($THETA)*X[]-Y[]-tan($THETA)*$X1)/sqrt((tan($THETA))**2+1))
            }
          }
        }
        fold::amr_sol'SolutionField{
          setfield W'quiescent
          setfield W'post_shock X[]<$Xs
        }
        fold::amr_sol'MeshAdaption{
          adaption  on
          lmax      $lmax
          r         $r
        }
        fold::amr_sol'RefinementCriteria{
          DensityGradient
          setflags [ooo|oxo|ooo] ON_BODY[]
        }
        makefield {G$lmax}
      end proc
    }
  }
}
```

```
  foreach method (roe_fl) # godunov_km, roe_fl, ausm_km, efm_km, hlle_km
    plugin amr_sol
    logfile logs/$method
    solver  code/$method
    fold::amrita { init plotting
    autoscale
    postscript on
    }
set r= 4
set gamma= 1.2
do angle= 14,20,2
do Ms= 5,10,1
  InertShockReflectionProblem {
    fold::amrita { parameters
          gamma = $gamma
      THETA #= rad($angle)
          Ms   = $Ms
          r = $r
    }
  }
  do phase=1,5, 1
    echo $phase
    echo $Ms
    echo $angle
    echo $gamma
    march 40 steps with cfl=0.8
    fold::amrita { schlieren
      plotfile ps/r$r/$method/gamma$gamma/THETA$angle/Mach$Ms/sch$phase.ps
        PlotDomain
        #DensityGradientPlot
        SchlierenImage
        DrawObstacleBody
      plotfile
    }
    fold::amrita { density
      plotfile ps/r$r/$method/gamma$gamma/THETA$angle/Mach$Ms/dens$phase.ps
        PlotDomain
        DensityPlot
        DrawObstacleBody
      plotfile
    }
    fold::amrita { pressure
      plotfile ps/r$r/$method/gamma$gamma/THETA$angle/Mach$Ms/press$phase.ps
        PlotDomain
        PressurePlot
        DrawObstacleBody
      plotfile
    }
    fold::amrita {pressure along ramp
      do t=32,120,1/16
        set w#=((tan(THETA)*$t)-(tan(THETA)*32))
            probe P[] at  $t,$w -> p
        fold::print {
           fold> file.=results/r$r/$method/gamma$gamma/THETA$angle/Mach$Ms/phase$phase
           $t $w $p
        }
```

```
     end do
    }
  end do
end do
end do
  end foreach
}
```

## Appendix B: MATLAB script used for analytical bifurcation prediction

The MATLAB script used to determine under what parameters $v_2$-$v_2$=$v_{3n}$ is shown here. It is based on the analytical approach presented in Section 2.1.2, with additional shock jump relations applied (see Thompson (1972)) in order to obtain the velocities. For a given $M_s$, $\theta_w$, and $\gamma$, an initial value of $\chi$ must be guessed (called $\chi_1$ in the script), and the script iterates to find the value of $\chi$ which satisfies the pressure condition across the slip line. For a given $\theta_w$ and $\gamma$, $M_s$ can be manually varied to find the conditions for which $v_2$-$v_2$=$v_{3n}$.

```
%% This program finds the value of chi (within 0.01 degrees) for a given Ms,
%% ramp angle, and gamma. It also calculates the velocities after each shock and
%% thus vn3 and v2-v3 are obtained and can be compared. The pressures in
%% region 2 and 3 are output to verify that the script is getting a reasonable
%% solution.
function u = transition6b(Ms,thetaw,gamma,chi1)
%% Triple point path angle loop
chi=chi1-0.01;%initial condition for the loop
P_rat2=5;%initial condition for the loop
P_rat3=0;%initial condition for the loop
P0=1; %initial pressure
p0=1; %initial density
while P_rat2-P_rat3>0
chi=chi+0.01;
%% Determining the flow strength after the incident shock
phi1=90-thetaw-chi;
M0=Ms/sind(phi1);
Mn1 = sqrt((1+(gamma-1)/2*(M0*sind(phi1))^2)/(gamma*(M0*sind(phi1))^2-(gamma-1)/2));
theta1 = [atand(2/tand(phi1)*(((M0*sind(phi1))^2-1)/(M0^2*(gamma+cosd(2*phi1))+2)))];
M1 = Mn1/sind(phi1-theta1);
P_rat1 = 1 +2*gamma/(gamma+1)*((M0*sind(phi1))^2-1);
T_rat1 = (1 +0.5*(gamma-1)*(M0*sind(phi1))^2)*((2*gamma*(M0*sind(phi1))^2/(gamma-1))-1)/(((gamma+1)^2*(M0*sind(phi1))^2)/(2*(gamma-1)));
p_rat1 = P_rat1/T_rat1;
P1=P_rat1*P0;
p1=p_rat1*p0;
c1=((gamma*P1)/(p1))^0.5;
v1=M1*c1;
%% Determining the flow strength after the Mach stem
phi3=90-chi;
Mn3 = sqrt((1+(gamma-1)/2*(M0*sind(phi3))^2)/(gamma*(M0*sind(phi3))^2-(gamma-1)/2));
theta3 = [atand(2/tand(phi3)*(((M0*sind(phi3))^2-1)/(M0^2*(gamma+cosd(2*phi3))+2)))];
M3 = Mn3/sind(phi3-theta3);
P_rat3 = 1 +2*gamma/(gamma+1)*((M0*sind(phi3))^2-1);
T_rat3 = (1 +0.5*(gamma-1)*(M0*sind(phi3))^2)*((2*gamma*(M0*sind(phi3))^2/(gamma-1))-1)/(((gamma+1)^2*(M0*sind(phi3))^2)/(2*(gamma-1)));
p_rat3 = P_rat3/T_rat3;
P3=P_rat3*P0;
p3=p_rat3*p0;
c3=((gamma*P3)/(p3))^0.5;
v3=M3*c3;
```

```
vn3=Mn3*c3;
%% Determining the flow strength after the reflected shock
phi2 = asind(1/M1);
theta2=theta1-theta3;
theta2l=0;
while theta2l-theta2<0
    phi2=phi2+0.01;
    theta2l = [atand(2/tand(phi2)*((M1^2*sind(phi2)^2-1)/(M1^2*(gamma+cosd(2*phi2))+2)))];
end
Mn2 = sqrt((1+(gamma-1)/2*(M1*sind(phi2))^2)/(gamma*(M1*sind(phi2))^2-(gamma-1)/2));
M2 = Mn2/sind(phi2-theta2);
P_rat2 = ((1 +2*gamma/(gamma+1)*((M1*sind(phi2))^2-1)))*P_rat1;
T_rat2 = T_rat1*(1 +0.5*(gamma-1)*(M1*sind(phi2))^2)*((2*gamma*(M1*sind(phi2))^2/(gamma-1))-1)/(((gamma+1)^2*(M1*sind(phi2))^2)/(2*(gamma-1)));
p_rat2 = p_rat1*((T_rat1*P_rat2)/(T_rat2*P_rat1));
P2=P_rat2*P0;
p2=p_rat2*p0;
c2=((gamma*P2)/(p2))^0.5;
v2=M2*c2;
%% end of loop
end
if phi2>90
    fprintf('increase your chi guess\n!');
else
    if chi<=chi1;
    fprintf('decrease your chi guess\n!');
    else
    chi
    vn3
    v2_v3=v2-v3
    P_rat2
    P_rat3
    end
End
```

# Appendix C AMRITA script for cellular detonation simulations

The AMRITA scripts used for the cellular detonation simulation are shown below. Script 1 was the first script used, and it followed the detonation to the end of the channel. It output a density plot and a soot foil every 50 time steps. It also output and saved the entire solution every 50 time steps (see line 328 of Script 1). In order to study the triple point reflections more closely, Script 2 was used to output a density plot and the “frontprofile.dat” file every time step. The input for Script 2 was one of the output solutions from Script 1 (see line 316 of Script 2). The “frontprofile.dat” output file contains information about the shock front location, as well as the pressure jump across the shock, from which the Mach number of the shock can be determined from the shock jump relations (see Thompson (1972).

## *Script 1*

```
1       fold::amrita { run simulation
2         fold::amrita { prelims
3           ReactiveEulerEquations {
4             space = 2D
5             add2W = VORT,E_RATE
6           }
7           fold::amrita { init resources
8             fold::amrita { assign sufficient resources
9               fold::amrita { define array sizes
10                ArraySizes {
11      #               NL     = 10       # maximum number of grid levels
12      #               NGD    = 2800     # maximum number of mesh patches
13      #               NGIJ   = 70000    # maximum number of perimeter cells
14      #               NGIxJ  = 200000   # maximum number of grid cells
15      #               NEX    = 2000     # length of external boundaries table
16      #               NBDYS  = 8000     # maximum number of scrunched boundaries
17      #               NGHOST = 2        # number of ghost cells
18                  NGIxJ=2500000
19                  NEX=40000
20                  NGD=8000
21                  NGIJ=100000
22                }
23              }
24            }
25            fold::amrita { get 1step
26              if(!&amrso("code/1step")) then
27                fold::amrita { build code
28                  fold::amrita { generate auxcode
29                    fold::print { soot_trace
30                      fold>file=code/soot_trace,recursion off,dollar off
31                      fold::amrita { daisy chain Ls2
32                        AddIntegrationStep {
33                          step = soot  (aka Ls2)  :record_vort(IM,JM,NG,DX,DY,W)
34                        }
```

```
    set amrita:bcg::integration .= *Ls2
  }
  fold::print {  record_vort
    *
    *
    *    RECORD_VORT:
    *
    *
        SUBROUTINE RECORD_VORT(IM,JM,NG,DX,DY,W)
    #include "$amrita:bcg::commonblk"
        AMRINT IM,JM,NG
        AMRDBL DX,DY
        AMRDBL W(NW,amrCpatch(IM,JM,NG))
        DO I=1,IM
          DO J=1,JM
            DUDY = (W(2,I,J+1)/W(1,I,J+1)
       X          -W(2,I,J-1)/W(1,I,J-1))/(2*DY)
            DVDX = (W(3,I+1,J)/W(1,I+1,J)
       X          -W(3,I-1,J)/W(1,I-1,J))/(2*DX)
            VORT = DVDX-DUDY
            IF(ABS(VORT).GE.ABS(W(6,I,J))) THEN
              W(6,I,J) = ABS(VORT)
            ENDIF
          END DO
        END DO
        RETURN
        END
  }
}
fold::print { energy_release
  fold>file=code/energy_release,recursion off,dollar off
  fold::amrita { daisy chain Ls3
    AddIntegrationStep {
      step = energy_release_rate  (aka Ls3)  :record_e_rate(IM,JM,NG,DX,DY,W)
    }
    set amrita:bcg::integration .= *Ls3
  }
  fold::print {  record_e_rate
    *
    *
    *    RECORD_E_RATE:
    *
    *
        SUBROUTINE RECORD_E_RATE(IM,JM,NG,DX,DY,W)
    #include "$amrita:bcg::commonblk"
        AMRINT IM,JM,NG
        AMRDBL DX,DY
        AMRDBL W(NW,amrCpatch(IM,JM,NG))
        CALL AMR::GET_CONST('amrita:EquationSet:expr::GAMMA',GMz)
        CALL AMR::GET_CONST('amrita:EquationSet:expr::Q',Qz)
        CALL AMR::GET_CONST('amrita:EquationSet:expr::E',Ez)
        DO I=1,IM
          DO J=1,JM
            P = (GMz-1)*(W(4,I,J)-0.5*(W(2,I,J)**2+W(3,I,J)**2)/W(1,I,J)-W(5,I,J)*Qz)
            RHO_DZDT = -W(1,I,J)*W(5,I,J)*EXP(-Ez*W(1,I,J)/P)
            IF(ABS(RHO_DZDT).GE.ABS(W(7,I,J))) THEN
```

```
                      W(7,I,J) = ABS(RHO_DZDT)
                    ENDIF
                  END DO
                END DO
                RETURN
                END
          }
        }
      }
      BasicCodeGenerator {
        solver = 1step
        scheme = roe'$znd::model
        auxcode= code/soot_trace,code/energy_release
      }
      fold::amrita { use minmod
        set solver::PHI = 1
        set solver::Pact= 1.1
        export solver::{PHI,Pact}
      }
    }
  endif
}
fold::amrita { define Cells
  proc Cells {
     fold::amrita { parameters
       gamma      =    1.2    # ratio of specific heats
       d  [0:?]   =    1.0     # overdrive
       Q  [0:50]  =     50     # heat release
       E  [0:50]  =     27     # activation energy
       lmax       =      2     # maximum number of grid levels
       r          =      2     # refinement ratio
       Npts[0:?]  =     64     # mesh points in half-reaction length
       Xd         =    30.0    # fix position of detonation
       piston_face=   -1E10     # trick interp with -infinity
       Ztol       = 0.005
       io         = .
       profiles  "= $io/znd/Q=$Q/E=$E/d=$d
       im         =    1000      # base grid points in x-direction
       jm         =    20       # base grid points in y-direction
       npatches   =     1
       ls         =    1.0
       b1         =    0.1       # ampplitude of lamda disturbance
       b2         =    4        # width of disturbance in x-direction
       xc         =    40        # position of disturbance band
     }
    }
    fold::amr_sol'Domain{
      lscale 1
      do n=1,$npatches
        patch <+,1,w$im,h$jm>
      end do
    }
    fold::amr_sol'SolutionField{
      fold::amrita { fix problem specfic quantities
        specify GAMMA ::= $gamma
        specify Q     ::= $Q
```

```
        specify E     ::= $E
       }
      fold::amrita { get W'znd
        fold::amrita { get znd
          ComputeZndProfile {
            rtn      = znd
            profiles = $profiles
          }
        }
        Xd     ::= X[]-($ls*$Xd)
        RM       ::= interp($znd.RHO,Xd[])
        UM       ::= interp($znd.U  ,Xd[])
        PM      ::= interp($znd.P  ,Xd[])
        ZM      ::= interp($znd.Z  ,Xd[])
      }
      setfield <RHO=RM[],U=UM[],V=0,P=PM[],Z=ZM[]>
      W'disturbance ::= <RHO=1.0,U=0, V=0, P=1, Z=1-$b1*rand(2)>
      zone ::= (abs(X[]-$xc)<$b2/2)
      setfield W'disturbance zone[]
    }
    fold::amrita { BoundaryConditions
      fold::amrita { get W'piston
        RB       ::= interp($znd.RHO,$piston_face)
        UB       ::= interp($znd.U  ,$piston_face)
        PB      ::= interp($znd.P  ,$piston_face)
        ZB      ::= interp($znd.Z  ,$piston_face)
        W'piston ::= <RHO=RB[],U=UB[],V=0,P=PB[],Z=ZB[]>
      }
      fold::amr_sol'BoundaryConditions{
        Nbdy  domain: reflect
        Ebdy  domain: extrapolate linearly
        Wbdy  domain: prescribe W'piston
        Sbdy  domain: reflect
      }
    }
    fold::amr_sol'MeshAdaption{
      adaption  on
      lmax      $lmax
      r         $r
    }
    fold::amr_sol'RefinementCriteria{
        fold::amrita{ for density gradient
          setflags [xxx|xxx|xxx] abs(RHO[+i]-RHO[])>0.1
          setflags [xxx|xxx|xxx] abs(RHO[+j]-RHO[])>0.1
        }
        fold::amrita{ for reaction zone
          setflags [ooo|oxo|ooo] Z[]>0.05 && RHO[]>2.0
          setflags [ooo|oxx|ooo] abs(RHO[+i]-RHO[])>0.0001 && abs(Z[]>0.99)
          setflags [oxo|oxo|ooo] abs(RHO[+j]-RHO[])>0.0001 && abs(Z[]>0.99)
          setflags [ooo|oxo|ooo] abs(Z[+i]-Z[])>$Ztol
          setflags [ooo|oxo|ooo] abs(Z[+j]-Z[])>$Ztol
        }
    }
    makefield {G$lmax}
  end proc
}
```

```
fold::amrita { diagnostics
  fold::amrita { define SootTraceImage
    proc SootTraceImage {
        fold::amrita { parameters
          SOOT             = W::VORT # what to plot
          grid             = {G}     # select grid
          min              = 0
          max              = 35
        }
      }
      wt          ::= 1 - abs(($SOOT[]-$min)/($max-$min))
      greyshading ::= wt[]>0 ? wt[] : 0
      plot image $grid m<greyshading[]>
    end proc
  }
  fold::amrita{ define DensityGradientPlot
    proc DensityGradientPlot {
        exposure [0:1]     = 1.0  # darkness of image
        grid               = {G}  # select grid
        max                = 2.
        min                = 0.
        }
        DrhoDx      ::= (RHO[+i]-RHO[-i])/(X[+i]-X[-i])
        DrhoDy      ::= (RHO[+j]-RHO[-j])/(Y[+j]-Y[-j])
        schlieren   ::= sqrt(DrhoDx[]**2+DrhoDy[]**2)
        wt          ::= 1-((schlieren[]-$min)/($max-$min))
        wt          ::= wt[]>0 ? wt[] : 0
        greyshading ::= $exposure*wt[]
        plot image $grid m<greyshading[]>
    end proc
  }
  fold::amrita{ define DensityPlot
    proc DensityPlot {
        exposure [0:1]     = 1.0  # darkness of image
        grid               = {G}  # select grid
        max                = 6.0
        min                = 0
        }
        wt          ::= 1-((RHO[]-$min)/($max-$min))
        wt          ::= wt[]>0 ? wt[] : 0
        greyshading ::= $exposure*wt[]
        plot image $grid m<greyshading[]>
    end proc
  }
  fold::amrita{ define PPlot
    proc PPlot {
        exposure [0:1]     = 1.0  # darkness of image
        grid               = {G}  # select grid
        max                = 20
        min                = 0
        }
        wt          ::= 1-((P[]-$min)/($max-$min))
        wt          ::= wt[]>0 ? wt[] : 0
        greyshading ::= $exposure*wt[]
        plot image $grid m<greyshading[]>
    end proc
```

```
      }
      fold::amrita{ define Z Plot
        proc ZPlot {
            exposure [0:1]     = 1.0  # darkness of image
            amplification [0:?]=  15  # magnification of weak features
            grid               = {G}  # select grid
            max                 = 1.0
            min                = 0
            }
            wt          ::= (Z[]-$min)/($max-$min)
            greyshading ::= $exposure*wt[]
            plot image $grid m<greyshading[]>
         end proc
      }
      fold::amrita{ define DzdtPlot
        proc DzdtPlot {
            DZDT               = W::E_RATE # what to plot
            exposure [0:1]     = 1       # darkness of image
            grid               = {G}     # select grid
            maxscale           = 1.33
            order              = 2
            tol              = 0.75     # threshold for amp1 amp2
            #amp1              = 0.2     # weak   features
            #amp2              = 0.25    # strong features
            amp1             = 1.0     # weak   features
            amp2             = 1.0    # strong features
            Ea               = 28
            }
            minmax log10($DZDT[]) -> min, max
            echo logmax $max
            wt          ::= (log10($DZDT[])-($maxscale-$order))/$order
            greyshading ::= wt[]>0 ? wt[] : 0
            plot image $grid m<$exposure*greyshading[]>
            end proc
      }
    }
  }
  plugin amr_sol
  Cells {
    fold::amrita { parameters
      gamma      =     1.2     # ratio of specific heats
      Q          =     50     # heat release
      E          =     27      # activation energy
      lmax       =      3      # maximum number of grid levels
      r          =      4      # refinement ratio
    }
  }
  fold::amrita { init plotting
    autoscale
    postscript on
  }
}
logfile logs/1step
solver  code/1step
#flowin io/modelxxx
do phase=0,100
```

```
    march 50 steps with cfl=0.5
    fold::amrita { density
      plotfile ps/dens$phase.ps
        PlotDomain
        DensityPlot
      plotfile
    }
    fold::amrita { soot foil
      plotfile ps/sootfoil$phase.ps
        PlotDomain
        SootTraceImage
      plotfile
    }
    flowout io/model$phase
  end do
}
```

## *Script 2*

```
fold::amrita { run simulation
  fold::amrita { prelims
    ReactiveEulerEquations {
      space = 2D
      add2W = VORT,E_RATE
    }
    fold::amrita { init resources
      fold::amrita { assign sufficient resources
        fold::amrita { define array sizes
          ArraySizes {
#             NL     = 10        # maximum number of grid levels
#             NGD    = 2800      # maximum number of mesh patches
#             NGIJ   = 70000     # maximum number of perimeter cells
#             NGIxJ  = 200000    # maximum number of grid cells
#             NEX    = 2000      # length of external boundaries table
#             NBDYS  = 8000      # maximum number of scrunched boundaries
#             NGHOST = 2         # number of ghost cells
            NGIxJ=2500000
            NEX=40000
            NGD=8000
            NGIJ=100000
          }
        }
      }
      fold::amrita { get 1step
        if(!&amrso("code/1step")) then
          fold::amrita { build code
            fold::amrita { generate auxcode
              fold::print { soot_trace
                fold>file=code/soot_trace,recursion off,dollar off
                fold::amrita { daisy chain Ls2
                  AddIntegrationStep {
                    step = soot  (aka Ls2)  :record_vort(IM,JM,NG,DX,DY,W)
```

```
    }
    set amrita:bcg::integration .= *Ls2
  }
  fold::print {  record_vort
    *
    *
    *     RECORD_VORT:
    *
    *
        SUBROUTINE RECORD_VORT(IM,JM,NG,DX,DY,W)
    #include "$amrita:bcg::commonblk"
        AMRINT IM,JM,NG
        AMRDBL DX,DY
        AMRDBL W(NW,amrCpatch(IM,JM,NG))
        DO I=1,IM
          DO J=1,JM
            DUDY = (W(2,I,J+1)/W(1,I,J+1)
       X           -W(2,I,J-1)/W(1,I,J-1))/(2*DY)
            DVDX = (W(3,I+1,J)/W(1,I+1,J)
       X           -W(3,I-1,J)/W(1,I-1,J))/(2*DX)
            VORT = DVDX-DUDY
            IF(ABS(VORT).GE.ABS(W(6,I,J))) THEN
              W(6,I,J) = ABS(VORT)
            ENDIF
          END DO
        END DO
        RETURN
        END
  }
}
fold::print { energy_release
  fold>file=code/energy_release,recursion off,dollar off
  fold::amrita { daisy chain Ls3
    AddIntegrationStep {
      step = energy_release_rate  (aka Ls3)  :record_e_rate(IM,JM,NG,DX,DY,W)
    }
    set amrita:bcg::integration .= *Ls3
  }
  fold::print {  record_e_rate
    *
    *
    *     RECORD_E_RATE:
    *
    *
        SUBROUTINE RECORD_E_RATE(IM,JM,NG,DX,DY,W)
    #include "$amrita:bcg::commonblk"
        AMRINT IM,JM,NG
        AMRDBL DX,DY
        AMRDBL W(NW,amrCpatch(IM,JM,NG))
        CALL AMR::GET_CONST('amrita:EquationSet:expr::GAMMA',GMz)
        CALL AMR::GET_CONST('amrita:EquationSet:expr::Q',Qz)
        CALL AMR::GET_CONST('amrita:EquationSet:expr::E',Ez)
        DO I=1,IM
          DO J=1,JM
            P = (GMz-1)*(W(4,I,J)-0.5*(W(2,I,J)**2+W(3,I,J)**2)/W(1,I,J)-W(5,I,J)*Qz)
            RHO_DZDT = -W(1,I,J)*W(5,I,J)*EXP(-Ez*W(1,I,J)/P)
```

```
                    IF(ABS(RHO_DZDT).GE.ABS(W(7,I,J))) THEN
                      W(7,I,J) = ABS(RHO_DZDT)
                    ENDIF
                  END DO
                END DO
                RETURN
                END
          }
        }
      }
      BasicCodeGenerator {
        solver = 1step
        scheme = roe'$znd::model
        auxcode= code/soot_trace,code/energy_release
      }
      fold::amrita { use minmod
        set solver::PHI = 1
        set solver::Pact= 1.1
        export solver::{PHI,Pact}
      }
    }
  endif
}
fold::amrita { define Cells
  proc Cells {
     fold::amrita { parameters
       gamma      =    1.2     # ratio of specific heats
       d  [0:?]   =    1.0     # overdrive
       Q  [0:50]  =     50     # heat release
       E  [0:50]  =     27     # activation energy
       lmax       =      2     # maximum number of grid levels
       r          =      2     # refinement ratio
       Npts[0:?]  =     64     # mesh points in half-reaction length
       Xd         =   30.0     # fix position of detonation
       piston_face=   -1E10    # trick interp with -infinity
       Ztol       = 0.005
       io         = .
       profiles  "= $io/znd/Q=$Q/E=$E/d=$d
       im         =   1000     # base grid points in x-direction
       jm         =    20      # base grid points in y-direction
       npatches   =     1
       ls         =   1.0
       b1         =   0.1      # ampplitude of lamda disturbance
       b2         =   4        # width of disturbance in x-direction
       xc         =   40       # position of disturbance band
     }
    }
    fold::amr_sol'Domain{
      lscale 1
      do n=1,$npatches
        patch <+,1,w$im,h$jm>
      end do
    }
    fold::amr_sol'SolutionField{
      fold::amrita { fix problem specfic quantities
        specify GAMMA ::= $gamma
```

```
      specify Q     ::= $Q
      specify E     ::= $E
     }
    fold::amrita { get W'znd
      fold::amrita { get znd
        ComputeZndProfile {
          rtn      = znd
          profiles = $profiles
        }
       }
       Xd     ::= X[]-($ls*$Xd)
       RM       ::= interp($znd.RHO,Xd[])
       UM       ::= interp($znd.U  ,Xd[])
       PM       ::= interp($znd.P  ,Xd[])
       ZM       ::= interp($znd.Z  ,Xd[])
    }
    setfield <RHO=RM[],U=UM[],V=0,P=PM[],Z=ZM[]>
    W'disturbance ::= <RHO=1.0,U=0, V=0, P=1, Z=1-$b1*rand(2)>
    zone ::= (abs(X[]-$xc)<$b2/2)
    setfield W'disturbance zone[]
  }
  fold::amrita { BoundaryConditions
    fold::amrita { get W'piston
      RB       ::= interp($znd.RHO,$piston_face)
      UB       ::= interp($znd.U  ,$piston_face)
      PB       ::= interp($znd.P  ,$piston_face)
      ZB       ::= interp($znd.Z  ,$piston_face)
      W'piston ::= <RHO=RB[],U=UB[],V=0,P=PB[],Z=ZB[]>
    }
    fold::amr_sol'BoundaryConditions{
      Nbdy  domain: reflect
      Ebdy  domain: extrapolate linearly
      Wbdy  domain: prescribe W'piston
      Sbdy  domain: reflect
    }
  }
  fold::amr_sol'MeshAdaption{
    adaption  on
    lmax      $lmax
    r         $r
  }
  fold::amr_sol'RefinementCriteria{
      fold::amrita{ for density gradient
        setflags [xxx|xxx|xxx] abs(RHO[+i]-RHO[])>0.1
        setflags [xxx|xxx|xxx] abs(RHO[+j]-RHO[])>0.1
      }
      fold::amrita{ for reaction zone
        setflags [ooo|oxo|ooo] Z[]>0.05 && RHO[]>2.0
        setflags [ooo|oxx|ooo] abs(RHO[+i]-RHO[])>0.0001 && abs(Z[]>0.99)
        setflags [oxo|oxo|ooo] abs(RHO[+j]-RHO[])>0.0001 && abs(Z[]>0.99)
        setflags [ooo|oxo|ooo] abs(Z[+i]-Z[])>$Ztol
        setflags [ooo|oxo|ooo] abs(Z[+j]-Z[])>$Ztol
      }
  }
  makefield {G$lmax}
end proc
```

```
}
fold::amrita { diagnostics
  fold::amrita { define SootTraceImage
    proc SootTraceImage {
       fold::amrita { parameters
         SOOT            = W::VORT # what to plot
         exposure [0:1]    = 1      # darkness of image
         grid            = {G}    # select grid
         tol             = 0.2    # threshold for amp1 amp2
         amp1            = 0.5    # weak   features
         amp2            = 0.25   # strong features
       }
      }
      minmax $SOOT[] -> min, max
      wt          ::= abs(($SOOT[]-$min)/($max-$min))
      greyshading ::= wt[]<$tol? wt[]**$amp1 : wt[]**$amp2
      plot image $grid m<$exposure*greyshading[]>
    end proc
  }
  fold::amrita{ define DensityGradientPlot
    proc DensityGradientPlot {
       exposure [0:1]    = 1.0  # darkness of image
       grid            = {G}  # select grid
       max             = 2.
       min             = 0.
       }
       DrhoDx      ::= (RHO[+i]-RHO[-i])/(X[+i]-X[-i])
       DrhoDy      ::= (RHO[+j]-RHO[-j])/(Y[+j]-Y[-j])
       schlieren   ::= sqrt(DrhoDx[]**2+DrhoDy[]**2)
       wt          ::= 1-((schlieren[]-$min)/($max-$min))
       wt          ::= wt[]>0 ? wt[] : 0
       greyshading ::= $exposure*wt[]
       plot image $grid m<greyshading[]>
    end proc
  }
  fold::amrita{ define DensityPlot
    proc DensityPlot {
       exposure [0:1]    = 1.0  # darkness of image
       grid            = {G}  # select grid
       max             = 6.0
       min             = 0
       }
       wt          ::= 1-((RHO[]-$min)/($max-$min))
       wt          ::= wt[]>0 ? wt[] : 0
       greyshading ::= $exposure*wt[]
       plot image $grid m<greyshading[]>
    end proc
  }
  fold::amrita{ define PPlot
    proc PPlot {
       exposure [0:1]    = 1.0  # darkness of image
       grid            = {G}  # select grid
       max             = 20
       min             = 0
       }
       wt          ::= 1-((P[]-$min)/($max-$min))
```

```
           wt          ::= wt[]>0 ? wt[] : 0
           greyshading ::= $exposure*wt[]
           plot image $grid m<greyshading[]>
        end proc
      }
      fold::amrita{ define Z Plot
        proc ZPlot {
           exposure [0:1]     = 1.0  # darkness of image
           amplification [0:?]=  15  # magnification of weak features
           grid               = {G}  # select grid
           max                 = 1.0
           min                = 0
           }
           wt          ::= (Z[]-$min)/($max-$min)
           greyshading ::= $exposure*wt[]
           plot image $grid m<greyshading[]>
         end proc
      }
      fold::amrita{ define DzdtPlot
        proc DzdtPlot {
           DZDT               = W::E_RATE # what to plot
           exposure [0:1]     = 1       # darkness of image
           grid               = {G}     # select grid
           maxscale           = 1.33
           order              = 2
           tol                = 0.75    # threshold for amp1 amp2
           #amp1               = 0.2    # weak   features
           #amp2               = 0.25   # strong features
           amp1               = 1.0     # weak   features
           amp2               = 1.0    # strong features
           Ea                 = 28
           }
           minmax log10($DZDT[]) -> min, max
           echo logmax $max
           wt          ::= (log10($DZDT[])-($maxscale-$order))/$order
           greyshading ::= wt[]>0 ? wt[] : 0
           plot image $grid m<$exposure*greyshading[]>
           end proc
      }
    }
  }
  plugin amr_sol
  Cells {
    fold::amrita { parameters
      gamma      =     1.2     # ratio of specific heats
      Q          =      50     # heat release
      E          =      27      # activation energy
      lmax       =       3      # maximum number of grid levels
      r          =       4      # refinement ratio
    }
  }
  fold::amrita { init plotting
    autoscale
    postscript on
  }
}
```

```
  logfile logs/1step
  solver  code/1step
  flowin io/model66
  do phase=0, 250
    echo phase $phase
    march 1 steps with cfl=0.5
    do j=0,20-1/64, 1/64
      echo $phase $j
      fold::amrita{ frontprofile
        along y = $j locate last P[]>1.1 -> Xfront
        along y = $j maximum X[],P[] for ($Xfront-X[]) < .1 -> loc, val
        time -> t
        fold::print{ save to file
          fold> file.=frontprofile/frontmodel66step$phase.dat
          $loc $j $val $t
        }
      }
    end do
    fold::amrita { density
      plotfile ps/densmodel66step$phase.ps
        PlotDomain
        DensityPlot
      plotfile
    }
  end do
}
```

# Appendix D AMRITA script for inert shock reflection simulations conducted in part 2

The AMRITA script used for the inert shock reflections simulation in part 2 is shown below. The output file “triplepoint.dat” (see line 239) was used to track the Mach shock, as well as the pressure jump across the Mach shock.

```
1    fold::amrita { define array sizes
2         ArraySizes {
3              #NGIxJ=25000000
4              #NEX=4000000
5              #NGD=100000
6              #NGIJ=10000000
7
8              #NL     = 100       # maximum number of grid levels
9              #NGD    = 280000     # maximum number of mesh patches
10             #NGIJ   = 7000000    # maximum number of perimeter cells
11             #NGIxJ  = 2000000    # maximum number of grid cells
12             #NEX    = 200000     # length of external boundaries table
13             #NBDYS  = 800000     # maximum number of scrunched boundaries
14             #NGHOST = 20         # number of ghost cells
15
16             NGIxJ = 2000000
17             NGD   = 8000
18
19        }
20   }
21   fold::amrita { run simulation
22     fold::amrita { prelims
23       EulerEquations {
24         add2W = VORT
25       }
26       fold::amrita { init resources
27         fold::amrita { get roe_fl
28           if(!&amrso("code/roe_fl")) then
29             fold::amrita { build code
30               BasicCodeGenerator {
31                 solver = roe_fl
32                 scheme = flux-limited'operator-split
33               }
34             }
35             fold::amrita { use minmod
36               set solver::PHI = 1
37               set solver::Pact= 1.1
38               export solver::{PHI,Pact}
39             }
40           endif
41         }
42         fold::amrita { DrawRamp
43           proc DrawRamp {
44             X1 = 0
```

```
    X2 = 0
    Y2 = 0
    ls = 1
    }<-ParamSet::
    set X2#=($ParamSet::im)*($ParamSet::ls)
    set Y2#=tan($ParamSet::THETA)*($X2-$X1)
    AmritaBlue
    filled polygon $X1,0, $X2,0, $X2,$Y2
  end proc
}
fold::amrita { DrawObstacleBody
  proc DrawObstacleBody {
    }
    plot amr_sol:axs::PSI[] contours L0.0 m<0>
    red   ::= amr_sol:axs::PSI[]<0 ? -1 : 69
    green ::= amr_sol:axs::PSI[]<0 ? -1 : 110
    blue  ::= amr_sol:axs::PSI[]<0 ? -1 : 150
    plot image {g0} RGB<red[],green[],blue[]>
  end proc
}
fold::amrita{ DensityGradientPlot
  proc DensityGradientPlot {
      exposure [0:1]     = 1.0  # darkness of image
      grid               = {G}  # select grid
      max                = 2.
      min                = 0.
      }
      DrhoDx      ::= (RHO[+i]-RHO[-i])/(X[+i]-X[-i])
      DrhoDy      ::= (RHO[+j]-RHO[-j])/(Y[+j]-Y[-j])
      schlieren   ::= sqrt(DrhoDx[]**2+DrhoDy[]**2)
      wt          ::= 1-((schlieren[]-$min)/($max-$min))
      wt          ::= wt[]>0 ? wt[] : 0
      greyshading ::= $exposure*wt[]
      plot image $grid m<greyshading[]>
  end proc
}
fold::amrita{ DensityPlot
  proc DensityPlot {
      exposure [0:1]     = 1.0  # darkness of image
      grid               = {G}  # select grid
      max                = 6.0
      min                = 0
      }
      wt          ::= 1-((RHO[]-$min)/($max-$min))
      wt          ::= wt[]>0 ? wt[] : 0
      greyshading ::= $exposure*wt[]
      plot image $grid m<greyshading[]>
  end proc
}
fold::amrita{ PPlot
  proc PPlot {
      exposure [0:1]     = 1.0  # darkness of image
      grid               = {G}  # select grid
      max                = 20
      min                = 0
      }
```

```
            wt          ::= 1-((P[]-$min)/($max-$min))
            wt          ::= wt[]>0 ? wt[] : 0
            greyshading ::= $exposure*wt[]
           plot image $grid m<greyshading[]>
        end proc
      }
      fold::amrita { ShockRamp
        proc ShockRamp{
            fold::amrita { parameters
              gamma     =  1.2
              Ms        =  2.     # shock strength
              Xs        =  5.00   # shock position
              lmax      =  2      # grid levels
              r         =  2      # refinement ratio
              im        =  240    # base grid points in x-direction
              jm        =  68     # base grid points in y-direction
              ls       #=  1/16.    # scaling parameter (1/ls) gives number of grid points within unity lengh scale
              X1        =  10     # coordinates of the start of nozzle
              THETA    #=  rad(30)
            }
          }<-> ParamSet::
          fold::amr_sol'Domain{
            lscale    $ls
            patch <+,1,w$im,h$jm>
          }
          fold::amrita { Problem specific quantities
            specify GAMMA ::= $gamma
          }
          fold::amrita { Boundary Conditions
            W'quiescent  ::= <RHO=1,U=0,V=0,P=1>
            fold::amrita { get post-shock state
              ShockWave{
                 <- ParamSet::
                 Ms=$Ms
                 state1=quiescent
                 state2=post_shock
              }
            }
            fold::amr_sol'BoundaryConditions{
              Nbdy  domain: reflect
              Ebdy  domain: extrapolate
              Wbdy  domain: prescribe   W'post_shock
              Sbdy  domain: reflect
              fold::amrita { define PSI
                PSI ::= ((tan($THETA)*$ls*X[]-$ls*Y[]-
tan($THETA)*$ls*$X1)/sqrt((tan($THETA))**2+1))
              }
              AXS::InternalBoundary {
                 PSI = PSI[]
              }
            }
          }
          fold::amr_sol'SolutionField{
            setfield W'quiescent
            setfield W'post_shock X[]<$Xs
          }
```

```
        fold::amr_sol'MeshAdaption{
          adaption  on
          lmax      $lmax
          r         $r
        }
        fold::amr_sol'RefinementCriteria{
          DensityGradient
          setflags [ooo|oxo|ooo] ON_BODY[]
        }
        makefield {G$lmax}
      end proc
    }
    fold::amrita { SootTraceImage
      proc SootTraceImage {
         fold::amrita { parameters
           SOOT              = W::VORT # what to plot
           exposure [0:1]    = 1       # darkness of image
           grid              = {G}     # select grid
           tol               = 0.2     # threshold for amp1 amp2
           amp1              = 0.5     # weak   features
           amp2              = 0.25    # strong features
          }
        }
        minmax $SOOT[] -> min, max
        wt          ::= abs(($SOOT[]-$min)/($max-$min))
        greyshading ::= wt[]<$tol? wt[]**$amp1 : wt[]**$amp2
        plot image $grid m<$exposure*greyshading[]>
      end proc
    }
  }
  plugin amr_sol
  ShockRamp {
    fold::amrita { parameters
      gamma  = 1.2
      Ms     = 6.43 # overdriven detonation (d=1.07,Mcj=6.22)
      Xs     = 8.
      THETA    #=    rad(34)
      im        =   24      # number of grid points in x-direction on base grid
      jm        =   7       # number of grid points in y-direction on base grid
      ls       #=   1/1.    # scaling parameter (1/ls) gives number of grid points within unity lengh scale
      X1        =     16.      # start of ramp, in detonation half reaction length scales
      lmax   = 3
      r      = 4
    }
  }
  fold::amrita { init plotting
    logfile logs/roe_fl
    solver  code/roe_fl
    autoscale
    postscript on
  }
}
fold::amrita { grids
    plotfile ps/grid0.ps
      plot grids
      DrawObstacleBody
```

```
    plotfile
}
fold::amrita { march to the detonation interaction with the ramp
  set Xsh = 0
  echo $Xsh
  while ($Xsh < ($ParamSet::X1))
    march 1 steps with cfl=0.5
    set ytop #= ($ParamSet::jm -1)*($ParamSet::ls)
    along y=$ytop locate last P[]>1.1 -> Xsh
    echo $ParamSet::X1 $Xsh
  end while
}
do phase=1,30
    echo $phase
    march 1 steps with cfl=0.5
    fold::amrita{ measure various trajectories
      fold::amrita{ measure trajectory and pressure at triple point
         set window #= 7*($ParamSet::ls)/(($ParamSet::r)**($ParamSet::lmax))
         set ytop #= ($ParamSet::jm -1)*($ParamSet::ls)
         along y=$ytop locate last P[]>1.1 -> Xshk
         along y=$ytop maximum X[],P[] for ($Xshk-X[])<$window -> xtriple, pinc
         along x=$xtriple locate last P[]>$pinc*1.1 -> Yshk
         along x=$xtriple maximum Y[],P[] for ($Yshk-Y[])<$window -> ytriple, pref
         along x=$xtriple+$window locate last P[]>1.1 -> Yshk
         along x=$xtriple+$window maximum Y[],P[] for ($Yshk-Y[])<$window -> loc, pmach
         time -> t
         fold::print{
           fold> file.=results/triplepoint.dat
            $xtriple $ytriple $pinc $pref $pmach $t
         }
      }
      fold::amrita{ track the shock along the ramp
        set xinc #=($ParamSet::ls)/(($ParamSet::r)**($ParamSet::lmax))
        set xend #=($ParamSet::im-1)*($ParamSet::ls)
        do x=$xend,$ParamSet::X1,-$xinc
          set y #= (tan($ParamSet::THETA))*($x-$ParamSet::X1)
          probe P[] at $x,$y -> pm
          if ($pm>1.1) then
            set xm = $x
            set ym = $y
            exitloop
          endif
        end do
        set ymid #= ($ym + $ytriple)/2.
        echo $ymid
        along y=$ymid locate last P[]>1.1 -> Xshk
        along y=$ymid maximum X[],P[] for ($Xshk-X[])<$window -> xmid, pmach
        fold::print{
          fold> file.=results/midmachramp.dat
            $xmid $ymid $pmach $t
        }
      }

    }
  flowout io/model$phase
  fold::amrita { profiles along the ramp
```

```
      set xinc #=($ParamSet::ls)/(($ParamSet::r)**($ParamSet::lmax))
      set xend #=($ParamSet::im-1)*($ParamSet::ls)
      foreach Q (RHO,U,V,P)
        fold::print {
         fold> file=results/alongramp/$Q$phase
        }
        do x=$ParamSet::X1,$xend,$xinc
          set y #= (tan($ParamSet::THETA))*($x-$ParamSet::X1)
          probe $Q[] at $x,$y -> q
          time->t
          fold::print {
            fold> file.=results/alongramp/$Q$phase
            $x $y $q $t
          }
        end do
      end foreach
    }
    printfile results/undisturbed/p$phase
      along y=4 print X[],P[]
    fold::amrita { density
      plotfile ps/dens$phase.ps
        PlotDomain Twall=0.5
        DensityPlot max=20
        DrawRamp <- ParamSet::
      plotfile
    }
    fold::amrita { grids
      plotfile ps/grids$phase.ps
        plot grids
      plotfile
    }
  end do
}
```